Quasi resonance in a leaky waveguide?

Nili Harnik,[a] Volkmar Wirth,[b]

[a] *Porter School of the Environment and Earth Sciences, Tel Aviv University, Israel*

[b] *Institute for Atmospheric Physics, Johannes Gutenberg-University Mainz, Germany*

Corresponding author: Nili Harnik, harnik@tauex.tau.ac.il

ABSTRACT: Resonant amplification has been suggested to cause the occasional large amplitude undulations in the jet streams, central to several impactfull phenomena like blocking, sudden stratospheric warmings and extreme weather. One of the models used for establishing the role of resonant amplification is a barotropic β-plane model with a constant zonal mean flow. In this work we examine how a specified amount of meridional leakage of wave activity to the subtropics affects the quasi-resonant response to a meridionally localized, pure zonal wavenumber forcing. The main novelty of our analysis is the derivation of an analytical solution, with which we quantitatively examine the effects of a specified amount of waveguide-leakage, and compare it to the effects of damping. We further examine the effects of leakage on the resonance of a meridionally-concentrated jet, through numerical simulations that include a carefully-constructed sponge layer to the south of the jet waveguide. We find that that meridional leakage weakens the resonant response, similar to what damping does, namely, the amplification and zonal-phase change across resonance are weaker. Leakage also affects the horizontal wave structure equatorwards of the forcing, by introducing a westward phase tilt towards the subtropics. Damping, on the other hand makes the amplitude of the wave decrease away from the forcing on both its side with only a minor phase tilt. Overall, it is concluded that even quite a large wave leakage towards the equator does not necessarily preclude the possibility of quasi-resonant amplification, but earlier estimates which ignore this leakage by assuming two fully-reflecting turning latitudes overestimate the effect by a considerable margin.

SIGNIFICANCE STATEMENT: One of the main causes of extreme temperatures and extreme weather is a strong meandering of the jet stream, with the undulations remaining roughly fixed in space, allowing the extreme conditions to develop. One of the mechanisms that has been suggested for these undulations is quasi-resonance of stationary Rossby waves which propagate along the jet-stream waveguide. A main assumption in these studies is that the jet is a perfect waveguide, however, it is well known that Rossby waves on a sphere tend to propagate towards the equator, making the wave-guide leaky. In this study we examine how leaking of waves towards the tropics affects quasi-resonance, and whether it still allows large undulations like those leading to extreme events to form.

1. Introduction

Resonant amplification has been suggested as an explanation for the occasional appearance of large amplitude undulations in the jet streams ever since Rossby and collaborators (1939) formulated the equations for Rossby waves (Haurwitz 1940). For example, resonance has been suggested to play a role in the occurrence of blocking (e.g Tung and Lindzen 1979a,b; Tung 1979), sudden stratospheric warmings (e.g. Plumb 1981; Tung and Lindzen 1979a,b; Tung 1979; Esler et al. 2006), multiple flow regimes and corresponding low frequency variability (e.g Charney and DeVore 1979; Källén 1997; Jin and Ghil 1990; Luo 1997), and extreme weather (e.g Petoukhov et al. 2013; Coumou et al. 2014; Petoukhov et al. 2016; Stadtherr et al. 2016; Kornhuber et al. 2017a,b; Mann et al. 2017, 2018; Kornhuber et al. 2019).

To strictly establish that resonant amplification occurs in the atmosphere, we need to demonstrate that by varying an external parameter of the mean flow or forcing, we get sharp amplification of the forced wave due to its getting closer to being a normal mode, with a sharp π-phase change across the resonance. This is straight-forward using the barotropic and shallow-water beta-plane channel models introduced by Rossby and collaborators (1939); Rossby (1940). However, though able to account quite well for many of the features of the observed upper level flow, these models are too simplified to establish the role of resonance in realistic flows. First, the exact "tuning" needed for resonance is not as easy to form in a latitude-height varying zonal mean flow on a sphere, with possible critical layers, equatorwards wave refraction, vertical propagation into the stratosphere, and various forms of damping. Second, the exact tuning of the mean flow into a resonant state will necessarily be ruined once resonant waves grow enough to modify the mean flow.

Tung, in a series of papers (Tung and Lindzen 1979a,b; Tung 1979), systematically relaxed various of the tuning-related simplifications, and derived semi-analytical solutions showing the existence of quasi-normal modes under more realistic flow conditions, provided the modes are vertically trapped (see also Esler and Scott 2005). Various studies starting from Charney and DeVore (1979) addressed the issue of nonlinear mean-flow modification, along with various tuning-related simplifications, in a range of model complexities, and showed that resonance can occur through self-tuning, and shape the low frequency variability of the flow, by allowing multiple flow regimes to exist (e.g Pedlosky 1981; Plumb 1979, 1981; Jin and Ghil 1990; Luo 1997; Esler et al. 2006; Lutsko and Held 2016).

One aspect which has only partially or indirectly been addressed in the above studies is the effect of equatorward refraction. On the sphere, Rossby waves tend to refract towards the equator (Hoskins and Karoly 1981) where waves tend to break and be absorbed at a critical layer (Killworth and McIntyre 1985). Such a wave activity-leakage to the equator affects the ability of normal modes, and correspondingly resonance to form (Tung 1979; Källén 1997; Lutsko and Held 2016). We will focus on this effect here.

Leakage to the equator is particularly important if another simplification of idealized resonance studies is relaxed, namely, that the wave source and mean flow are zonally symmetric. If the wave source is localized in the zonal direction, the wave emanating from it needs to propagate around the globe to form a resonant mode (c.f. Lutsko and Held 2016). If the leakage to the equator is too strong, a circumglobal mode will not form. Thus, the existence of a zonal waveguide (e.g Hoskins and Ambrizzi 1993) is necessary for a normal mode to be established and resonantly excited. Various studies have developed diagnostics of the *waveguidability* of the flow, and used it to examine its dependence on parameters of the zonal mean flow (e.g Hoskins and Ambrizzi 1993; Branstator 2002; Manola et al. 2013; Wirth 2020). These studies all show that a strong localized zonal jet is needed to guide the waves zonally.

In this paper we will examine the role of meridional trapping in a simple model which allows an analytical solution. We note that Tung (1979) derived analytical normal mode solutions in the presence of a critical surface with linear damping. His solution shows that quasi-normal modes, and correspondingly quasi-resonance, do occur due to partial reflection. In that study, however, the amount of partial meridional reflection can't be controlled. In this study, we take a different approach, in which we use a very simple model (barotropic β-plane channel model with constant zonal flow) in which we specify the amount of wave-activity leakage to the tropics (model and analytical solution described in section 2). We then examine the effect of meridional leakage on resonance, how it compares with the effects of damping, and whether the combination of realistic amounts of leakage and damping allow a reasonable amount of quasi-resonance to explain realistic wave amplification (section 3). We further compare our results to carefully constructed numerical solutions of a barotropic channel model with a meridionally-localized zonal jet stream, and a leaky equatorial boundary (section 4), and summarize with a discussion of the relevance to more realistic flows in section 5. To facilitate the flow of the paper, some of the technical points are discussed in appendices.

2. Analytic solutions of a barotropic β-plane channel model

To incorporate leakage into an analytical forced wave solution, we use the simplest setup of a zonally-oriented Rossby wave guide, a β-plane channel model, with poleward and equatorward boundaries at $y = \pm L$, a constant zonal flow $\overline{u}$, and a meridionally localized (in the form of a δ-function) stationary wave forcing of a given zonal wavenumber. This δ-function forcing structure allows, via a Greens function method, to obtain analytical solutions for a partially reflecting southern channel boundary, which allows part of the wave activity to leak out. We will examine how linear drag and leakage through the equatorward boundary modify the amplitude and phase of the response to forcing, and specifically, how it modifies the resonant response, viewed by varying the strength of the zonal mean zonal wind across its resonant value.

a. Basic model and Greens function forcing setup

We assume a zonal mean zonal flow $\overline{u}$, with linear momentum damping α. We express the anomaly fields (deviation from a zonal mean) in terms of a streamfunction ψ, which satisfies $v = \frac{\partial \psi}{\partial x}$, $u = -\frac{\partial \psi}{\partial y}$, and $q = \frac{\partial v}{\partial x} - \frac{\partial u}{\partial y} = \frac{\partial^2 \psi}{\partial y^2} + \frac{\partial^2 \psi}{\partial x^2}$, where v, u, and q, are the meridional wind, the zonal wind and vorticity anomalies respectively, and t, x, and y are the time, zonal direction and meridional direction coordinates. The linearized vorticity equation with topography $h(x, y)$ as forcing is then:

$$\left(\frac{\partial}{\partial t}+\overline{u}\frac{\partial}{\partial x}+\alpha\right)\left(\frac{\partial^2\psi}{\partial y^2}+\frac{\partial^2\psi}{\partial x^2}\right)+\frac{\partial\psi}{\partial x}\overline{q}_y=-f_o\overline{u}\frac{\partial h}{\partial x} \tag{1}$$

where $\overline{q}_y=\beta-\frac{d^2\overline{u}}{dy^2}$ is the meridional gradient of the zonal-mean flow vorticity, and f_o is the central channel Coriolis force.

To allow for an analytical solution, we will assume a constant zonal-mean zonal flow $\overline{u}=U$, and use a Green's function approach, where we examine the response $G_k(y,y')$, to a pure sinosodial topography in the zonal direction, localized at a single latitude y' : $h(x,y)=\delta(y-y')e^{ikx}$. The response to a general topography $h(x,y)$ can then be obtained by taking a Fourier transform in the zonal direction, and for each zonal component, convolving the response to the Green's function with the full forcing at zonal wavenumber k:

$$\psi_k(y)=\int_{-L}^{L}G_k(y,y')h_k(y')dy' \tag{2}$$

where $h_k(y)$ is the Fourier component k of the topography $h(x,y)$. In what follows we will examine a single zonal Fourier mode and drop the subscript k.

Looking for steady solutions (to fit the stationary forcing), we assume a solution of the form:

$$\psi(x,y)=G(y,y')e^{ikx}$$

Plugging in to equation 1, after taking into account that $\overline{u}(y)=U=const$ (which yields $\overline{q}_y=\beta$), we are left with solving the following equation:

$$\frac{d^2G}{dy^2}+\left(\frac{\beta}{U-\frac{i\alpha}{k}}-k^2\right)G=-\frac{f_o}{1-\frac{i\alpha}{kU}}\delta(y-y') \tag{3}$$

Away from the forcing latitude y', the solution will be that of the homogeneous problem, and will assume the form $e^{i\tilde{l}y}$, $e^{-i\tilde{l}y}$ where

$$\tilde{l}^2=\frac{\beta}{U-\frac{i\alpha}{k}}-k^2 \tag{4}$$

For the inviscid case, we get $\tilde{l}(\alpha = 0) = l$ where

$$l = \sqrt{\frac{\beta}{U} - k^2} \tag{5}$$

In appendix 5 we show that the corresponding complex meridional wavenumber approximately equals:

$$\tilde{l} \approx l + \frac{i\alpha}{Cg_y} \tag{6}$$

where $Cg_y = \frac{2kl\beta}{(k^2+l^2)^2}$ is the meridional group speed[1]. Note that for a wave solution, we need l to be real, meaning $\frac{\beta}{U} > k^2$.

The full solution is then comprised of two parts, equatorwards and polewards of the forcing:

$$G(y, y') = \begin{cases} A_1 e^{i\tilde{l}y} + A_2 e^{-i\tilde{l}y} & y > y' \\ \\ B_1 e^{i\tilde{l}y} + B_2 e^{-i\tilde{l}y} & y < y' \end{cases} \tag{7}$$

and the meridional EP flux, which represents the meridional flux of wave activity, equals:

$$F_{(y)} = -\overline{uv} = -\frac{1}{2}\Re(uv^*) \approx \frac{k}{2} \begin{cases} l\left(|A_1|^2 e^{-\frac{2\alpha}{Cg_y}y} - |A_2|^2 e^{\frac{2\alpha}{Cg_y}y}\right) - \frac{2\alpha}{Cg_y}\Im\left(A_1 A_2^* e^{2ily}\right) & y > y' \\ \\ l\left(|B_1|^2 e^{-\frac{2\alpha}{Cg_y}y} - |B_2|^2 e^{\frac{2\alpha}{Cg_y}y}\right) - \frac{2\alpha}{Cg_y}\Im\left(B_1 B_2^* e^{2ily}\right) & y < y' \end{cases} \tag{8}$$

where $\Re$ and $\Im$ denote the real and imaginary components, and the approximation of $\tilde{l}$ for small α (equation 6) was assumed. Physically, $F_{(y)}$ is the sum of a poleward (A_1, B_1) and equatorward (A_2, B_2) propagating waves, with the temporal decay at rate α resulting in a spatial decay rate of $\frac{\alpha}{Cg_y}$, with an additional component (the imaginary term) which arises due to the effect of the damping on the phase of the waves (via the effect on $\tilde{l}$).

The coefficients $A_{1,2}$ and $B_{1,2}$ need to be determined from the boundary conditions at $y = \pm L$, and from the following matching conditions at $y = y'$, implemented by taking the limit of ϵ going

---

[1]Note that the group *speed* is by definition positive. Here we choose the convention that l is positive, and the wave solution is $e^{\pm i\tilde{l}y}$. Under this convention, the poleward propagating part of the wave is proportional to $e^{ily}e^{-\frac{\alpha}{Cg_y}y}$, which decays polewards, while the equatorward propagating part of the solution is proportional to $e^{-ily}e^{\frac{\alpha}{Cg_y}y}$, which decays equatorwards.

to zero:

$$\lim_{\epsilon \to 0} (G(y' + \epsilon, y') - G(y' - \epsilon, y')) = 0$$
$$\lim_{\epsilon \to 0} \left(\frac{dG}{dy}|_{y'+\epsilon} - \frac{dG}{dy}|_{y'-\epsilon} \right) = -\frac{f_0}{1 - \frac{i\alpha}{kU}} \tag{9}$$

The first matching condition insures continuity of pressure and meridional flow, and the second condition is obtained by integrating equation 3 in y.

b. Boundary conditions incorporating leakage

The simple boundary condition of no meridional flow into across the channel walls implies $G(\pm L, y') = 0$. We will assume this always holds at the poleward boundary $y = L$. This implies $A_2 = -A_1 e^{i2\tilde{l}L}$, which yields

$$G(y > y', y') = A \left(e^{i\tilde{l}(y-L)} - e^{-i\tilde{l}(y-L)} \right) \tag{10}$$

where $A \equiv A_1 e^{i\tilde{l}L}$.

The vanishing of the streamfunction at the walls implies full reflection of waves from it. This is seen by implementing the rigid wall boundary condition (equation 10) into the meridional component of the Eliassen-Palm (EP) flux (Eq. 8):

$$F_{(y)}(y > y') \approx kl|A|^2 \sinh\left(\frac{2\alpha}{Cg_y}(y-L)\right) + \frac{k\alpha}{Cg_y}\sin(2l(y-L)) \tag{11}$$

which vanishes at $y = L$. Note that in the case of inviscid flow, $F_{(y)} = 0$ everywhere, not just at the boundaries, consistent with the polewards and equatorwards components having equal amplitudes, resulting in a zero net meridional wave activity flux.

To incorporate leakage of wave activity at the southern boundary, we start from the expression for the wave activity flux at the southern part of the channel for the inviscid case (setting $\alpha = 0$ in equation 8):

$$F_{(y)}(y < y') = \frac{kl}{2}(|B_1|^2 - |B_2|^2) \tag{12}$$

This solution, which is similar to that derived by Harnik (2001), indicates that $F_{(y)}$ is constant when there is no damping. When some of the wave activity leaks through the equatorward boundary, the poleward reflected wave has a smaller amplitude than the incident wave, resulting in a net EP flux out of the domain. This can be explicitly imposed, by setting:

$$|B_1|^2 = |R|^2 |B_2|^2$$

where $|R|^2 \leq 1$ is the amount of wave activity reflected back polewards from the southern channel boundary. From equation 12, the meridional EP flux south of the wave source is negative, consistent with a net equatorward wave activity flux:

$$F_{(y)}(y < y') = -(1 - |R|^2)\frac{kl}{2}|B_2|^2$$

The quantity $1 - |R|^2$ denotes the fraction of wave activity leakage out of the waveguide.

Requiring that the meridional velocity at the boundary will vanish when there is full reflection ($|R| = 1$), we get the following condition on the solution coefficients

$$B_1 = -|R| e^{2i\tilde{l}L} B_2$$

and the following general solution

$$G(y, y') = \begin{cases} A\left(e^{i\tilde{l}(y-L)} - e^{-i\tilde{l}(y-L)}\right) & y > y' \\ \\ B\left(|R| e^{i\tilde{l}(y+L)} - e^{-i\tilde{l}(y+L)}\right) & y < y' \end{cases} \tag{13}$$

where we used $B \equiv -B_2 e^{i\tilde{l}L}$. Note that the meridional wind anomaly at the southern boundary is not zero when there is leakage of wave activity ($|R| \neq 1$), consistent with a membrane, rather than with a rigid wall.

This leaky boundary condition can also be phrased as the following condition at $y = -L$ (see Appendix 5 for a derivation):

$$\left(\frac{1 - |R|}{1 + |R|}\right)\frac{dG}{dy} + i\tilde{l}G = 0 \tag{14}$$

c. The full solution

Plugging solution 13 into the matching conditions 9, we get the leaky, damped, Green's function solution:

$$G(y,y') = \frac{i f_0}{2\tilde{l}(1-\frac{i\alpha}{kU})(e^{-2i\tilde{l}L}-|R|e^{2i\tilde{l}L})} \begin{cases} (e^{-i\tilde{l}(y'+L)}-|R|e^{i\tilde{l}(y'+L)})(e^{i\tilde{l}(y-L)}-e^{-i\tilde{l}(y-L)}) & y > y' \\ (e^{i\tilde{l}(y'-L)}-e^{-i\tilde{l}(y'-L)})(e^{-i\tilde{l}(y+L)}-|R|e^{i\tilde{l}(y+L)}) & y < y' \end{cases} \tag{15}$$

3. The effect of leakage and damping on resonance in the β-plane channel

In what follows, we will examine the physical properties of the analytical solution, specifically, how the resonance properties of the inviscid perfect-channel case are modified by wave activity leakage, and how its influence compares with the effect of damping.

a. Resonance in the inviscid perfect channel

To do this we will start by examining the resonant response to the δ-localized forcing in the case of a perfect waveguide. Setting $\alpha = 0$, $|R| = 1$ in equation 15 we get:

$$G(y,y') = -\frac{f_o}{l\sin(2lL)} \begin{cases} \sin(l(y'+L))\sin(l(y-L)) & y > y' \\ \sin(l(y'-L))\sin(l(y+L)) & y < y' \end{cases} \tag{16}$$

We see that the solution blows up if the parameters of the problem are such that $L = \frac{\pi}{2l}$, where the meridional wavenumber l, c.f. equation 5, is a function of the externally specified zonal mean zonal wind U, the meridional PV gradient β, and the topography zonal wavenumber k, and is independent of the channel width L. In this case, we have resonance, because the wave source excites waves which, after propagating polewards and equatorwards to the channel walls and getting reflected back, reach the source exactly in phase to enhance it.

Fig. 1 shows the amplitude and phase at $y = 0$, for the case of a mid-channel source $y' = 0$, as a function of the zonal wind U, for a given non-dimensional zonal wavenumber $s = k\frac{L_x}{2\pi}$, L_x being the zonal channel length, based on equation 16. We note that similar results can be obtained by varying other parameters, like the meridional channel width, or the zonal wavenumber, and for other channel-parameter values. The classical features of resonance are evident - the amplitude blows up, and there is a sharp phase shifting of π radians across the resonance, with the wave geopotential being exactly out of phase with the forcing height anomaly for sub-resonant zonal winds, and in phase with the forcing for super-resonant zonal winds, and the anomaly being exactly in quadrature with the mountain at resonance (c.f. Vallis 2017).

To examine the relevance of the resonance behavior of our point source solution to a more realistic, non-localized forcing, we compare to the response to a cosine-shaped mountain $h(x, y) = \cos(l_o y)e^{ikx}$, for which the analytical solution to equation 1 is easily shown to be:

$$\psi_k(y) = -\frac{f_o}{l^2 - l_o^2}\left(\cos(l_o y) - \frac{\cos(ly)\cos(l_o L)}{\cos(lL)}\right) \tag{17}$$

where as before, l satisfies equation 5. In appendix B1, we show how this solution is obtained using the Greens function approach, by plugging expression 16 for $G(y, y')$ into equation 2.

We note a few things:

- The first term in the parentheses is the particular solution for the $\cos(l_o y)$ forcing, while the second term is a homogeneous solution, which is added to insure that the boundary condition $\psi'(x, \pm L) = 0$ is satisfied for any l_o.

- As for the Green's function solution, the homogeneous part of the solution here also blows up (resonance) when the flow parameters (k and U) yield a meridional wavenumber which is equal to $l = \frac{\pi}{2L}$.

- For flow parameters which yield a meridional wavenumber equal to that of the forcing ($l = l_o$), but is not resonant in the sense above ($l \neq \frac{\pi}{2L}$), both the term in brackets, and the denominator $l^2 - l_o^2$ are zero, and we get the following finite solution (using l'Hôpital's Rule):

$$\lim_{l \to l_o} \psi_k(y) = -f_o \frac{y\sin(l_o y)\cos(l_o L) - L\sin(l_o L)\cos(l_o y)}{2l_o\cos(l_o L)}$$

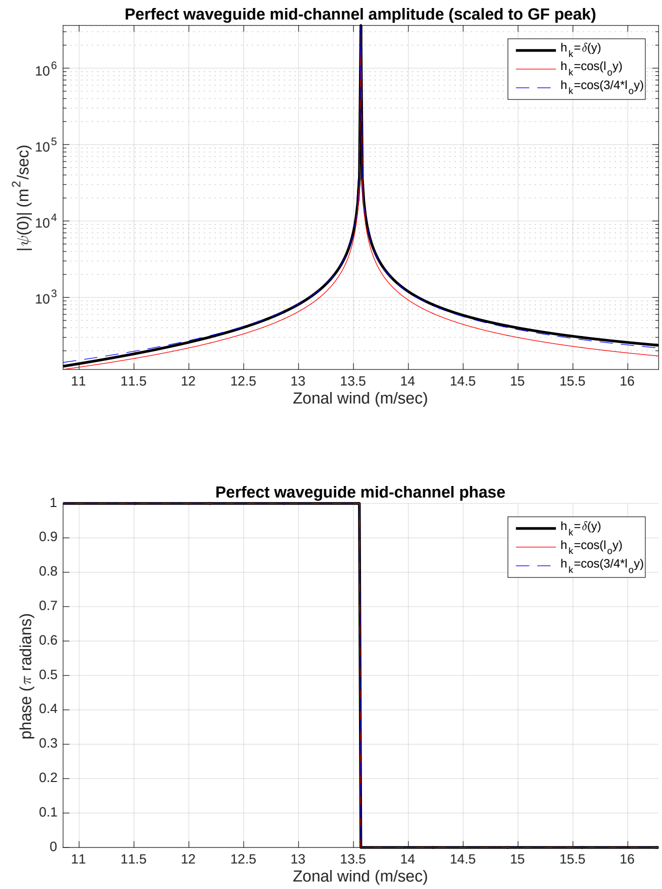

FIG. 1. The amplitude (top) and phase (relative to the forcing zonal phase, in units of π, bottom) of the mid-channel streamfunction for three different forcing shapes: $h_k(y) = \delta(y)$ (thick black), $h_k(y) = \cos(l_o y)$ (red), and $h_k(y) = \cos(\frac{3}{4} l_o y)$ (dashed blue), for $l_o = \frac{\pi}{2L}$, as a function of the zonal mean zonal wind (U), for non dimensional zonal wavenumber $s = 4$ at latitude $\phi_0 = 40^o$, with the channel half-width $L_o = 2000 km$, which gives a resonant zonal mean zonal wind value of $U_0 = 13.57 m/sec$. For plotting purposes, we offset the value of U by a tiny amount ($10^{-5} m/sec$) from resonance values, for the peak to be finite. Note that the y-axis is logarithmic. For comparison between the different forcing shapes, the solutions were normalized by the integral of the forcing over the channel, giving resonance-peak values of the $\cos(l_o y)$ and $\cos(3/4 l_o y)$ solutions of 0.79 and 0.99 of the $\delta(y)$ solution peak, respectively.

Note that this solution vanishes at the boundaries $y = \pm L$, but in general, it is not resonant because the forcing structure, though a solution to equation 1, does not, in itself, satisfy the boundary conditions.

- When the forcing is chosen to vanish at the channel walls - $l_o = \frac{\pi}{2L}$ - the second term in the parentheses of 17 is zero, yielding the more commonly discussed forced solution (e.g Petoukhov et al. 2013):
$$\psi_k(y) = -\frac{f_o \cos(l_o y)}{l^2 - l_o^2}$$
and when the flow parameters are such that $l = l_o$, we get resonance. In this case the forcing has the structure of the free solution of equation 1 and the boundary conditions, meaning it is a normal mode of the system.

The mid-channel amplitude for the cosine-forcing case is also shown in Fig. 1 (thin line). Comparing the responses to the point-source and cosine forcing shapes, we see a very similar dependence on U. The above results suggest the delta-forcing solution can be used to study the resonance properties of the system, which are not too sensitive to the meridional shape of the forcing, as long as it excites a normal mode of the system[2].

b. The resonant response in the presence of damping

Keeping α finite and plugging $|R| = 1$ in solution 15 gives:

$$G(y,y') = \frac{i f_0}{2\tilde{l}(1 - \frac{i\alpha}{kU})(e^{2i\tilde{l}L} - e^{-2i\tilde{l}L})} \begin{cases} (e^{i\tilde{l}(y'+L)} - e^{-i\tilde{l}(y'+L)})(e^{i\tilde{l}(y-L)} - e^{-i\tilde{l}(y-L)}) & y > y' \\ \\ (e^{i\tilde{l}(y'-L)} - e^{-i\tilde{l}(y'-L)})(e^{i\tilde{l}(y+L)} - e^{-i\tilde{l}(y+L)}) & y < y' \end{cases} \tag{18}$$

In analogy to the inviscid case, we also obtain the following solution for a cosine forcing (see appendix B1):

$$\psi_k(y) = -\frac{f_o}{\frac{\beta}{U} - (l_o^2 + k^2)(1 - \frac{i\alpha}{kU})} \left(\cos(l_o y) - \frac{\cos(l_o L)(e^{i\tilde{l}y} + e^{-i\tilde{l}y})}{(e^{i\tilde{l}L} + e^{-i\tilde{l}L})} \right) \tag{19}$$

---

[2]There is one caveat to this statement. Under very specific conditions, the δ-forcing parameters can result in a destructive, rather than a constructive interference of the reflected waves with the source. This appears as "anti-resonance" points, for which the amplitude sharply decreases to zero. Such points do not appear in the cosine-forcing case because this cancellation happens for the forcing at a single latitude, so that forcings from different latitudes take over the response. The destructive interference point, as well as higher order resonances occur outside the domain of zonal wind values shown in Fig. 1, and are discussed in Section e.

We note first that in the inviscid limit, $\tilde{l}(\alpha = 0) = l$, and 18, 19 converge to 16, 17. Fig. 2 shows the mid-channel amplitude and phase dependence on U, for the case of a delta-forcing at mid channel ($y = 0$), as well as for the cosine forcing with $l_o = \frac{\pi}{2L}$, for a few values of the damping parameter. We see that for non vanishing α, the solution is no longer singular, though it is strongly amplified at the inviscid-resonance U value, with a sharp phase shifting of almost π radians. The quasi-resonant amplification, and the sharpness and amount of phase shifting decrease with the damping rate. We also see that for large enough damping (damping time scales smaller than 16 days), the resonance peak shifts to larger values of U, corresponding to narrower resonant channel widths. We also see, as in the conservative channel case, the shape of the resonance for a δ forcing is very similar to that of a cosine forcing.

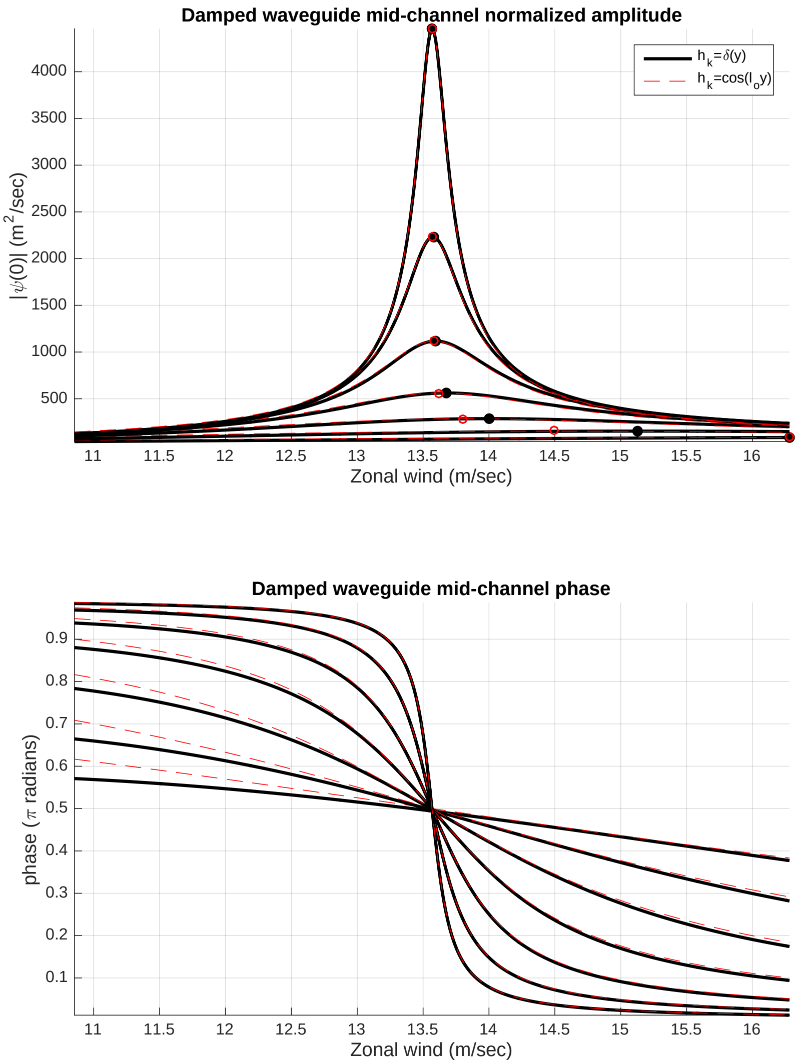

FIG. 2. As in figure 1 but for a model with damping, for a forcing shape $h_k(y) = \delta(y)$ (black) and $h_k(y) = \cos(l_o y)$ (red dashed), for different damping values, corresponding to damping time scales of 2, 4, 8, 16, 32, 64, 128 days. The damping strength affects the profiles in a monotonous way, with the peak amplitude increasing as the damping gets weaker (a longer damping time scale), and the phase change around the resonance peak getting sharper as the damping is reduced. The filled black/open red circles mark the peak amplitude for each profile. The channel and flow parameters are similar to those of figure 1.

c. The effect of leakage on the resonant response

To examine the effects of leakage, we start with the case of no damping. Setting $\alpha = 0$ in solution 15 we get:

$$G(y,y') = -\frac{f_0}{l(e^{-2ilL} - |R|e^{2ilL})} \begin{cases} \sin l(y-L)\,(e^{-il(y'+L)} - |R|e^{il(y'+L)}) & y > y' \\ \\ \sin l(y'-L)\,(e^{-il(y+L)} - |R|e^{il(y+L)}) & y < y' \end{cases} \tag{20}$$

Fig. 3 shows the mid-channel response to a Delta-function forcing at $y' = 0$, for $|R|^2$ ranging between 0.95 to 0 (leakage ranging from 5-100 percent). We see a clear indication for quasi-resonance (sharp amplification and almost-π phase shifting) for small leakage, with the peak amplification and phase shifting weakening and becoming wider as more wave activity leaks out. For the case of full leakage ($|R|^2 = 0$), there is no amplification and the phase of the solution changes linearly with U across the whole range.

The solution with no reflection from the southern boundary allows us to quantify the effect of resonance, by defining an amplitude amplification factor for a given $|R|$ as the ratio between the resonance-amplitude and the corresponding amplitude for $|R| = 0$. We also define a phase-change rate as the amount of phase change per change in U (in units of $\frac{\pi}{ms^{-1}}$). This value is largest (in absolute value) at the resonance peak. Table 1 shows the amplitude amplification factor and phase-change rate for solutions based on equation 20 (some of the runs are shown in Fig. 3). We see that the sensitivity to leakage is strongest near the pure resonance state, when there is very little leakage. However, even quite a lot of leakage (e.g. $|R|^2 = 0.25$) can result in an amplitude amplification which is significant (2.6 for $|R|^2 = 0.25$), which in the real atmosphere may be enough to lead to extreme weather. The phase-change rate also changes strongly with the amount of leakage. Thinking about a theoretical case in which a change in the mean flow of $1ms^{-1}$ leads to resonance, we will see a full change in phase of π radians for small leakage values (c.f. less than 25% - $|R|^2 > 0.75$), however, the phase change becomes quite small when the leakage is large, being less than $1/8^{th}$ of a wavelength for $|R|^2 = 0.25$. The rate of change of the wave phase with the mean flow velocity may be a useful quantity to examine in observations to detect the possibility of resonance.

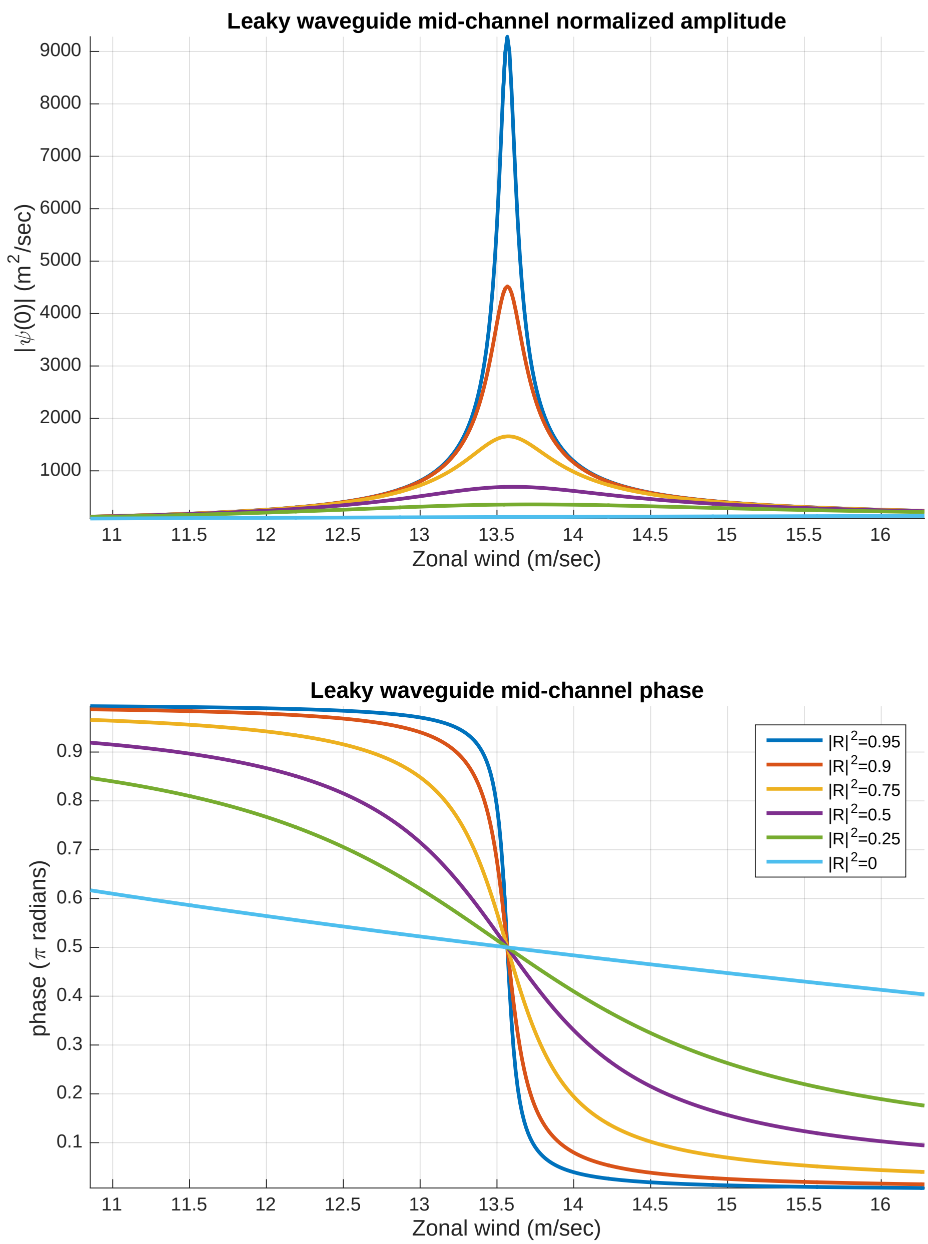

FIG. 3. As in figure 1 but for the leaky channel, for the forcing $h_k(y) = \delta(y)$. The reflection coefficient $|R|^2$ denotes the fraction of wave activity which is reflected back into the waveguide, while a fraction of $1-|R|^2$ leaks out of the southern boundary.

TABLE 1. The resonance amplitude-amplification factor and phase-change rate for different degrees of leakage $(1-|R|^2)$, for the leaky channel with no damping (the reflectivity values in bold are shown in Fig. 3). The phase change measure is the largest phase jump across two adjacent U values, and is shown in units of π radians per ms^{-1}.

Reflectivity $\|R\|^2$	**0.95**	**0.9**	0.8	**0.75**	0.7	**0.5**	0.4	**0.25**	0.2	0.1	**0**
Amplitude amplification	65.9	32.1	15.2	11.8	9.5	4.9	3.8	2.6	2.2	1.7	1
Phase-change rate $(\pi/(ms^{-1}))$	5.88	2.91	1.38	1.07	0.86	0.44	0.33	0.22	0.19	0.13	0.05

Comparing figures 2 and 3 suggests leakage and weak damping have a similar effect on resonance[3]. This similarity is expected since both processes act to reduce the wave activity as it propagates back and forth between the meridional channel walls. A more quantitative comparison can be made by estimating the damping rate in the leaky channel by assuming that each time the wave traverses across the channel and back (a distance of $4L$), a fraction $1-|R|^2$ of its wave activity leaks out. Taking into account that the wave activity propagates at the group velocity speed Cg_y, and noting that the streamfunction ψ decays at half the rate of the wave activity $A \propto q'^2 \propto \psi'^2$ ($\frac{1}{A}\frac{dA}{dt} \approx \frac{1}{2\psi}\frac{d\psi}{dt}$), we get an estimate of an effective leakage decay rate of:

$$\alpha_{Leaky} \approx \frac{1}{2}\frac{(1-|R|^2)Cg_y}{4L} \tag{21}$$

For values of $|R|^2 = [0.95, 0.9, 0.75, 0.5, 0.25, 0]$, and the parameters used to create Fig. 3, this gives damping time scales of $\tau \approx \alpha^{-1} = [8982, 2246, 359, 90, 40, 22.5]$ days. Fig. 4 shows a comparison of the mid-channel amplitude solutions as a function of the channel width, for $|R|^2 = 0.95$ and $|R|^2 = 0.5$, alongside the damped-channel solutions with α_{Leaky} taken from equation 21. We see that for the weak leakage, the damped-solution matches the leakage one really well. For stronger leakage, the differences become apparent, suggesting equation 21 under-estimates the equivalent effective damping rate (stronger damping is needed to make the red curves closer to the black curves, which show slower amplitude and phase changes near the resonance compared to the red curves).

An alternative quantitative measure to relate the effects of damping to leakage is by comparing the phase shifting across the resonance. Table 2 shows the phase change, as calculated in table 1,

[3]Note however that strong damping, unlike strong leakage, changes the value at which resonance occurs.

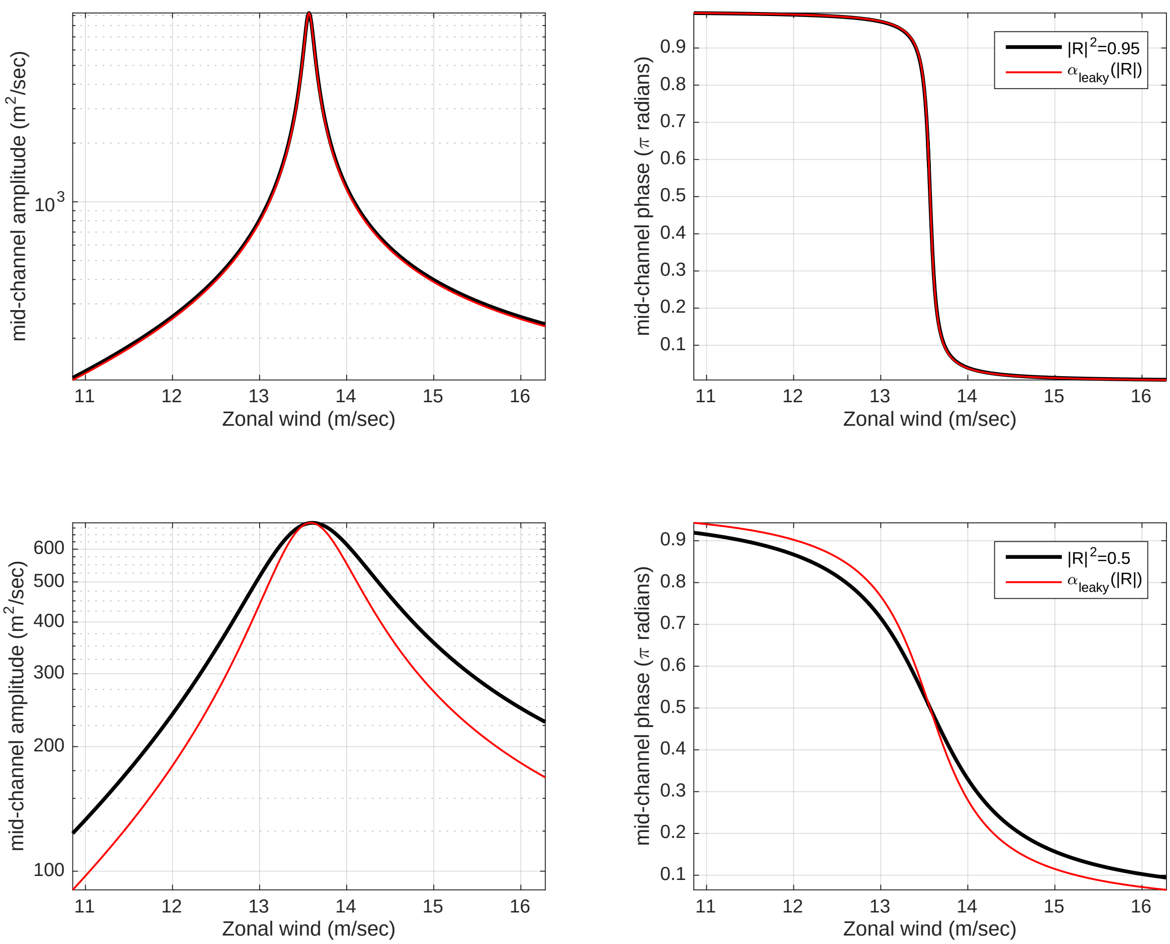

FIG. 4. The mid-channel amplitude for $|R|^2 = 0.95$ (top) and $|R|^2 = 0.5$ (bottom), similar to the curves shown in figure 3 (black contours), along with the damped-channel solutions (similar to Figure 2 but for the corresponding effective damping values given by equation 21.

for different damping values (calculated from equation 18, some values are shown in Fig. 2). By comparing the phase changes to those in table 1, we can see that leakage values of 5, 50 and 100 percent of the wave activity ($|R|^2 = 0.95, 0.5, 0$) correspond, respectively, to damping time scales of 256, 20 and 2 days.

TABLE 2. The resonance phase-change rate for different damping time scales (day^{-1}), for the runs calculated from equation 18. Damping times in bold are shown in Fig. 2.

Damping τ (days^{-1})	256	**128**	**64**	45	36	20	**16**	10	**8**	6	**2**
Phase-change rate ($\pi/(ms^{-1})$)	5.66	2.87	1.44	1.01	0.81	0.45	0.36	0.22	0.18	0.13	0.04

While the effect of damping and leakage on the resonant behaviour may be similar in terms of the amplitude and phase changes across the resonance values, the spatial mode structure is qualitatively different, as shown by Fig. 5. While poleward of the forcing the two wave fields look similar, equatorward of it, the damped solution is symmetric around the forcing while the leaky solution shows a south-west north east tilted wave which is nonzero at the channel wall. Correspondingly, the meridional EP flux is identically zero for the perfect waveguide. For the damped case it is directed away from the forcing (and symmetric for this mid-channel forcing location) with a value of zero at the walls, as required by the boundary conditions of perfect reflection. For the leaky case, on the other hand, it is piece-wise constant, with a value of zero poleward of the forcing and negative equatorward of the forcing, consistent with wave activity leakage out of the southern channel wall.

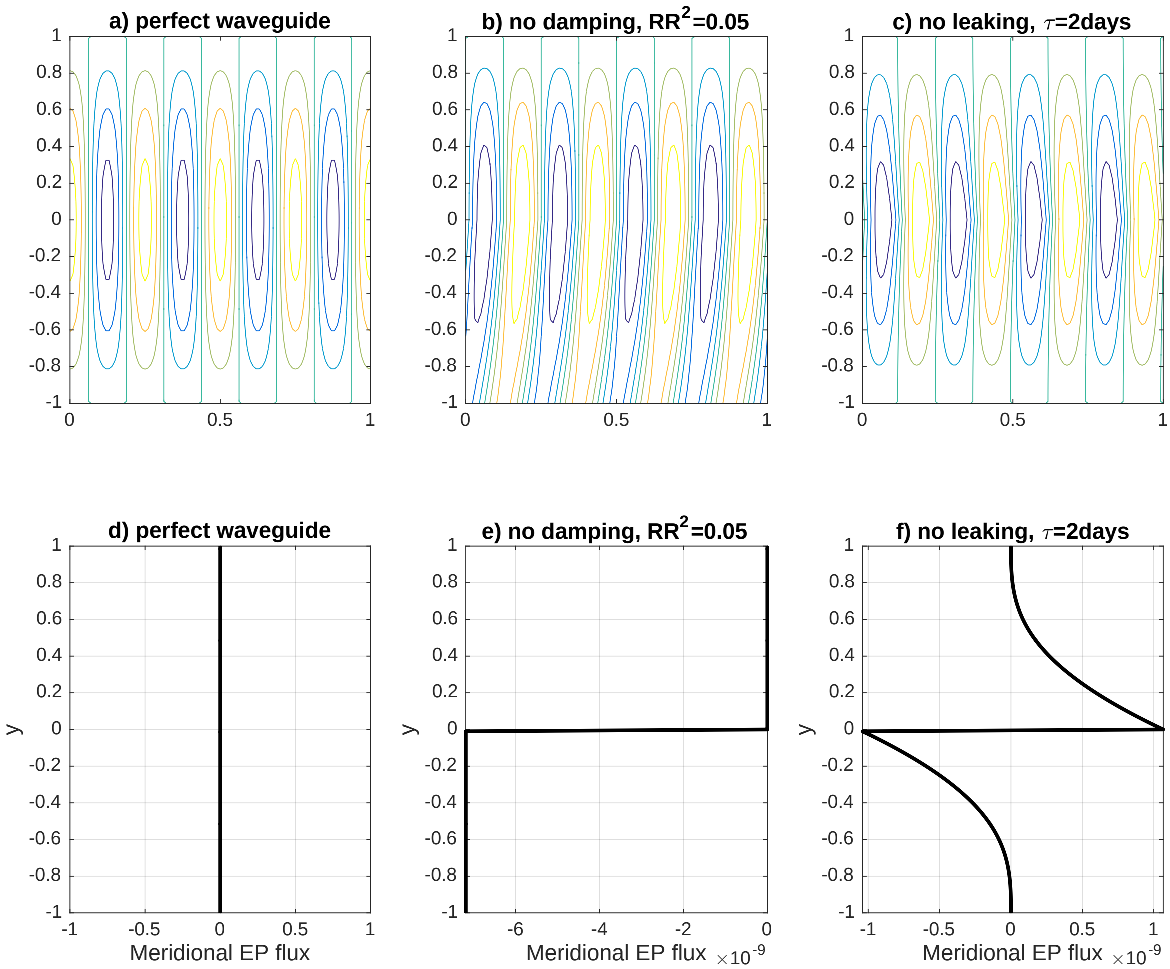

FIG. 5. The latitude-longitude structure of the stream-function (top row) and the meridional EP flux as a function of latitude (bottom row) in response to a delta forcing at the mid channel latitude ($y = 0$) for the following runs: a,d) A perfect channel (no damping and no leakage, see Figure 1). b,e) A leaky channel with $|R|^2 = 0.05$ and no damping (see Figure 3). c,f) A strongly damped channel ($\tau = 2d$) with no leakage (see Figure 2). Latitude is in units of L, the half-channel width. Longitude is is divided by the length of a latitude circle.

d. The combined effect of leakage and damping

Fig. 6 shows the solution at mid-channel for Delta-function forcing at mid-channel, for the same $|R|^2$ values shown in Fig. 3, for very weak (128 days) and stronger (8 days) damping rates. We see that damping acts to widen the quasi-resonance curves, and to reduce the sensitivity to weak amounts of leakage (e.g. the difference between the $|R|^2 = 0.95$ to $|R|^2 = 0.9$ curves is smaller for stronger damping). We also see that as with the damped perfect waveguide case, strong damping acts to shift the resonance peak to stronger zonal mean zonal winds (resonance occurs at larger U for a damping time scale of 8 days).

To further quantify the effects of damping and leakage when both exist, we examine the domain-integrated eddy kinetic energy (EKE) budget. A similar analysis could be done for other conserved quantities, e.g. enstrophy or wave activity, but we choose EKE because for a δ-function forcing, the PV perturbation is also a δ function and we want to avoid δ-squared terms. Multiplying the PV equation 1 by the complex-conjugate streamfunction ψ^*, and taking a domain average, gives in steady state (see Appendix B1):

$$\frac{\alpha}{\overline{u}}\left(EKE - \overline{u'\psi'}|_{-L}\right) + \overline{u'v'}|_{-L} = -f_o\overline{\tilde{h}v'(y')} \tag{22}$$

where EKE is the domain integrated eddy kinetic energy, and over-bar denotes a zonal mean, and $\tilde{h}$ is the zonally-varying amplitude of the topographic δ-forcing, $h = \tilde{h}\delta(y - y')$. Note that $\tilde{h}$ has a sinusoidal structure in the zonal direction, $\tilde{h} = h_o e^{ikx}$.

The equation tells us that EKE generation by the forcing (right hand side term) is balanced by dissipation of EKE and leakage of wave activity out of the southern boundary (first and second terms on the left hand side, respectively). The damping term includes a boundary contribution, which is non-zero when both damping and leakage exist (recall that $\psi'(-L) = 0$ when there is no leakage), however, we find that it is at least an order of magnitude smaller than the other terms, thus we can ignore it. An important point to note is that the forcing term depends on the zonal phasing between the meridional wind anomaly and the topography. When there is no damping or leakage, away from resonance, v' is in quadrature with the forcing (ψ' is in or out of phase with the forcing), meaning there is no EKE generation, and all terms in the equation are zero. Right at resonance, on the other hand, v' is in phase with h, so that the forcing does generate EKE, which,

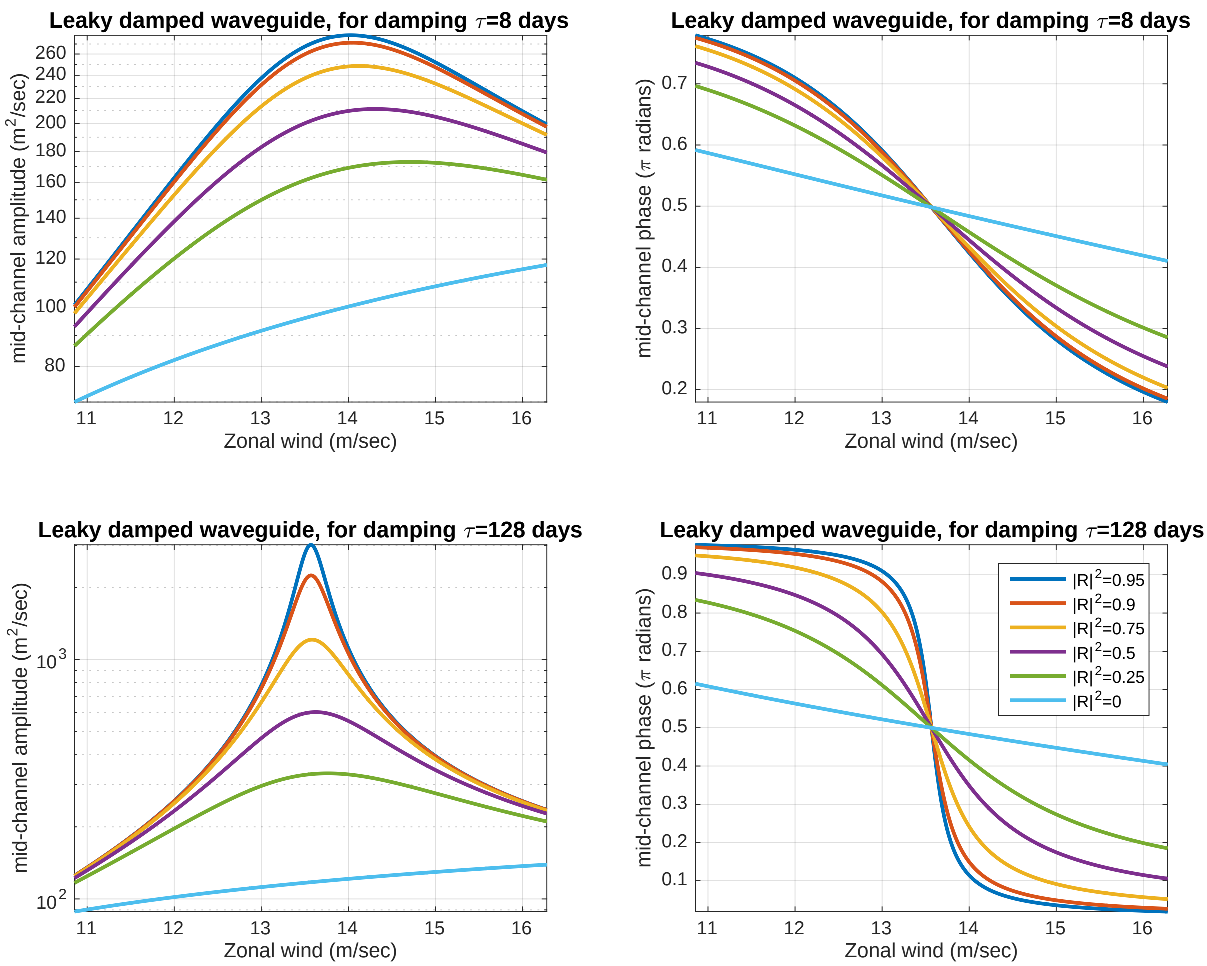

FIG. 6. Same as figure 3, but for damped leaky channel, for two values of damping: Top - 128days. Bottom - 16 days. Mid channel amplitude is on the left, and the mid-channel phase is on the right.

in the the absence of leakage and damping, must lead to a temporal growth of EKE (no steady state). Indeed, it is a known feature of resonant solutions that they give a linear amplitude growth of modes which, off-resonance, are not growing. Fig. 7 shows the EKE forcing term for two sets of runs, with varying degrees of leakage or damping. We see an opposite dependence of the EKE forcing strength on the magnitude of leakage/damping, for modes near or away from resonance. Near resonance, the EKE generation by the forcing is larger for smaller damping/leakage, while

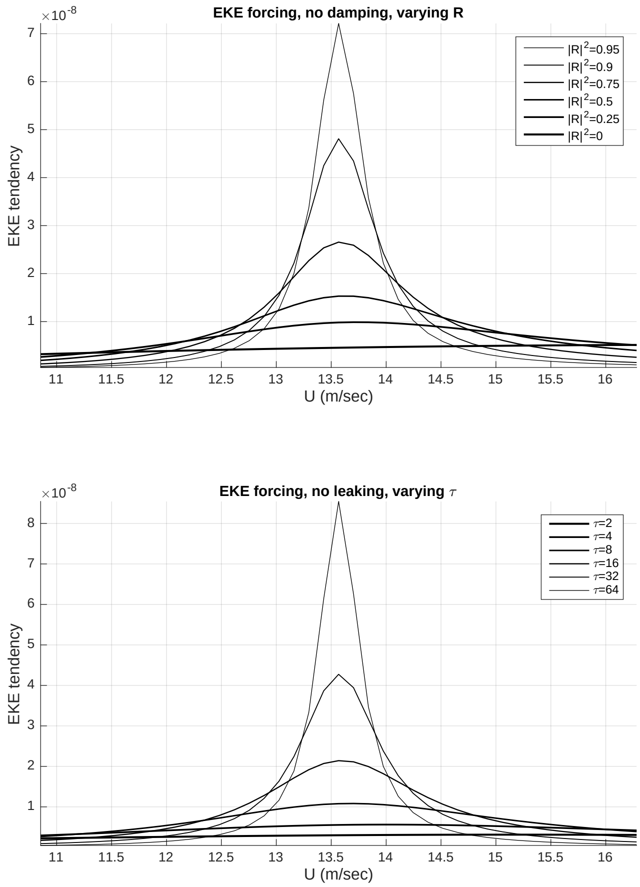

FIG. 7. The EKE forcing term (RHS of equation 22), for a) the leaky inviscid runs shown in figure 3. b) the damped non-leaky runs shown in figure 2.

well away from the resonance, this dependence changes, with a range of zonal wind values for which there is a non monotonic change of the EKE forcing magnitude with damping or leakage, with optimal forcing for a middle value.

e. Higher order resonances

The results shown so far pertain to the main resonance of the model, for which the nondimensional meridional wavenumber $n = l\frac{L}{\pi} = \frac{1}{2}$, meaning exactly half a wave-length fits into the channel width. For lower values of U, however, for which the meridional wavenumber is larger (c.f. equation 5), higher order resonances appear, for larger values of n. Fig. 8 shows the mid-channel amplitude and phase for a few combinations of leakage and damping (shown for a narrower range of U values in figures 1, 2, 3). The perfect channel case (thick black curves) shows a weaker resonance at $U = 2.82ms^{-1}$, and two "anti-resonance" points at which the amplitude decreases sharply towards $U = 5.56ms^{-1}$ and $U = 1.66ms^{-1}$. An examination of the horizontal structure of the waves shows that the second resonance occurs for $n = \frac{3}{2}$, while the "anti-resonance" points occur for $n = 1$ and $n = 2$, respectively.

Fig. 9, shows the horizontal structure of ψ' for the second resonance (plot g) and the first "anti-resonance" (plot a), as well as for a U value in between these two points (plot d). At resonance, the amplitude peaks at mid-channel. At "anti-resonance", on the other hand, the wave-node falls at mid-channel. Thus, while these meridional modes are free solutions of the homogeneous equation which also satisfy the boundary conditions, they are not really resonant, because the forcing does not project onto them in a way which keeps nudging them to grow once the mode has been established. This, however, is an artifact of the localized nature of the forcing at mid-channel, and we expect these modes to become resonant if the forcing will be placed off the channel center, or for a wider forcing.

Examining the effects of damping or leakage on the second resonance, we see that although the effect of damping and leakage at the secondary resonance looks similar when looking at the mid-channel amplitude and phase (red and blue curves in Fig. 8), it is very different on the mode structure (Fig. 9g,h,i). While strong damping makes the mode look similar to the primary resonance (compare figures 9g and 5c), leakage of wave activity from the southern boundary changes the structure of the wave only south of the forcing, where the main effect is westward phase tilt away from the forcing, along with an amplitude modification. The differences between leakage and damping is even more pronounced for the "anti-resonance" modes. While the special nature of this mode disappears for strong damping (the thick blue curves in Fig. 8 show no special behavior near these points), strong leakage shows a minimum mid-channel amplitude and EKE forcing,

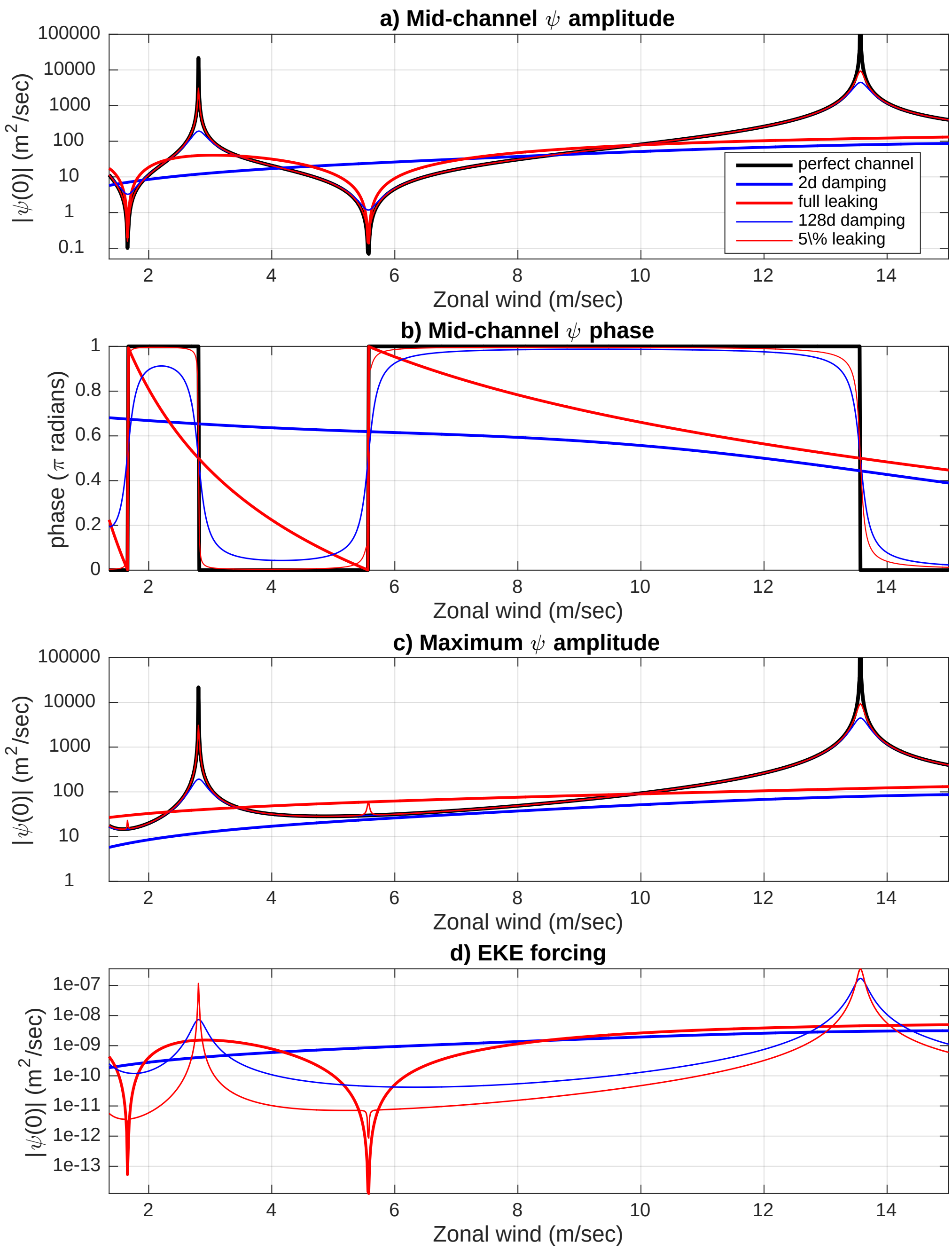

FIG. 8. The solution as a function of U. Shown are: a) the mid-channel streamfunction amplitude, b) the mid-channel streamfunction phase (in units of π), c) the channel-maximum streamfunction amplitude, d) the EKE forcing. Shown are results for a perfect channel (no leakage or damping, thick black), full leakage no damping ($|R|^2 = 0, \alpha = 0$, thick red), strong damping no leakage ($|R|^2 = 1, \alpha = 1/(2days)$, thick blue), weak damping no leakage ($|R|^2 = 1, \alpha = 1/(128days)$, thin blue), weak leakage no damping ($|R|^2 = 0, \alpha = 0$, thin red).

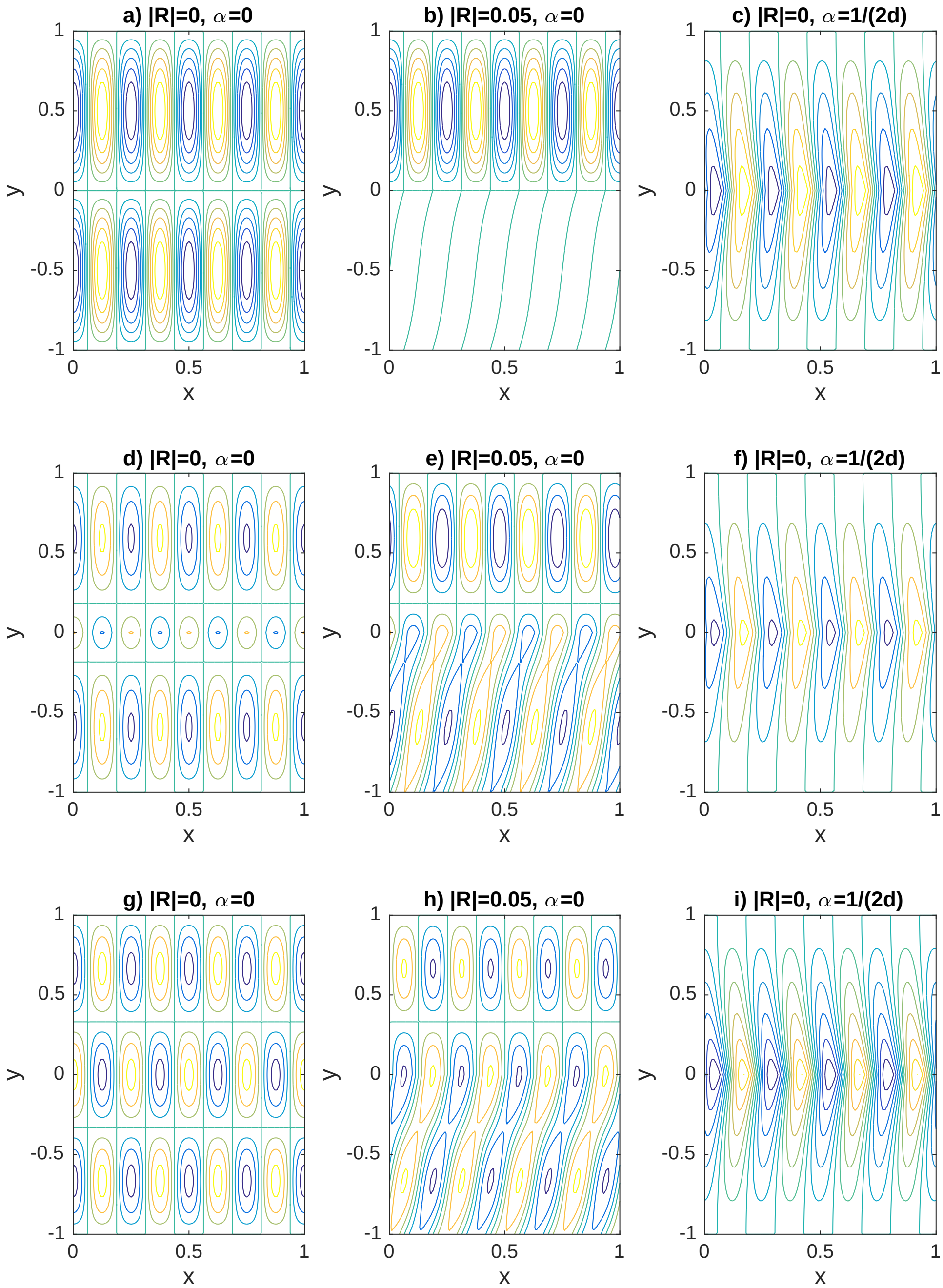

FIG. 9. The latitude-longitude structure of the stream-function for the second resonance, at $U = 5.56ms^{-1}$ (top row), for $U = 4ms^{-1}$, a mid value between the second and third resonance (middle), and the third resonance, at $U = 2.82ms^{-1}$ (bottom row) for the following runs: a,d,g) A perfect channel (no damping and no leakage, see Figure 1). b,e,h) A leaky channel with $|R|^2 = 0.05$ and no damping (see Figure 3). c,f,i) A strongly damped channel ($\tau = 2d$) with no leakage (see Figure 2). Latitude is in units of L, the half-channel width. Longitude is is divided by the length of a latitude circle.

and a π phase shift across these points (the thick red curves in Fig. 8). The π phase shifting is clearly understood when examining the horizontal structure of the streamfunction at the first anti-resonance for the perfect channel case ($U = 5.56ms^{-1}$, Fig. 9a), and for a slightly weaker zonal wind ($U = 4.0ms^{-1}$, Fig. 9d) - as U decreases, the meridional wavelength goes from half a wavelength being larger, to being smaller than half a channel width, resulting in a small oppositely phased peak at the channel center for the latter. Note that the anti-resonant mode for a perfect channel has a symmetric structure around the forcing, thus, it is not a pure standing mode structure with a node and a meridional π phase shift in mid channel. This suggests the forced mode should be viewed as consisting of two separate modes, to both sides of the channel. When the channel is fully leaky, the equatorward mode assumes a propagating wave structure (a westward phase tilt towards the southern channel wall), and at the anti-resonance point, where the EKE forcing becomes zero due to destructive interference, the equatorward part disappears (Fig. 9b).

The importance of these anti-resonance points is in pointing out a very strong sensitivity of the wave structure south of the forcing to the channel and forcing parameters, when the damping is weak enough. If relevant for more realistic settings, this might have implications for subtropical waves.

4. Numerical solutions

The solutions presented above allow a theoretical study of the linear stationary-wave response and resonance, in a very idealized channel, with a meridionally-localized forcing. We can use these analytical solutions to construct the solution to an arbitrary meridional forcing structure using equation 7, however, these solutions cannot be used when the zonal wind varies with latitude. Under more realistic settings of a jet-stream waveguide, the membrane-like leaky channel wall represents the subtropical turning latitude, which will allow partial tunneling to the tropics where the waves are damped. A systematic study the effect of leakage on quasi-resonance under more realistic conditions requires using a numerical model. To incorporate leakage, we will examine the numerical solution of a stationary wave channel model in which we have a sponge layer in the southern part of the domain to represent leakage.

The model solves equation 1 for meridionally varying zonal mean zonal flow $\overline{u}(y)$, damping $\alpha(y)$, and topography $h(x, y)$. Examining the response to the k'th zonal Fourier component $h_k(y)$, we get the following equation for the stream-function response ψ_k:

$$\left(1 - \frac{i\alpha}{k\overline{u}}\right) \frac{d^2\psi_k}{dy^2} + \left[\frac{\overline{q}_y}{\overline{u}} - \left(1 - \frac{i\alpha}{k\overline{u}}\right) k^2\right] \psi_k = -f_o h_k \ . \tag{23}$$

As boundary conditions we specify $\psi_k = 0$ at the northern and southern boundary of the computational domain. Eq. (23) is discretized with the help of standard centered differences, and the resulting matrix equation is solved using the python package `SciPy`. In the remainder of this paper we assume $\overline{u} > 0$ throughout the interior of the domain such that (23) is free of singularities. For later reference we define the square of the stationary wavenumber

$$K_s^2 = \frac{\overline{q}_y}{\overline{u}} \ , \tag{24}$$

and the dimensionless stationary wavenumber

$$\hat{K}_s = \frac{L_x}{2\pi} \sqrt{K_s^2} \ . \tag{25}$$

Our standard configuration is chosen very similar to that from the analytical treatment. In particular, we use a channel width of 4×10^3 km extending from $Y_{\mathrm{min}} = -2 \times 10^3$ km to $Y_{\mathrm{max}} = -2 \times 10^3$ km and a (dimensionless) zonal wavenumber $s = 4$. The meridional profile of the orography is specified as

$$h_k(y) = h_0 \cos^2\left(\frac{\pi\, y}{h_N - h_S}\right) \tag{26}$$

for $h_S \le y \le h_N$, and zero otherwise, with $h_S = -500$ km, $h_N = 500$ km, and $h_0 = 1$. By design, the meridional width of $h_k(y)$ is much smaller than the channel width, such that it is close to a delta function at $y = 0$ that we considered in our analytical treatment. At the same time, it is wide enough such that it is represented by a fair number of grid points and, hence, properly resolved in our numerical treatment.

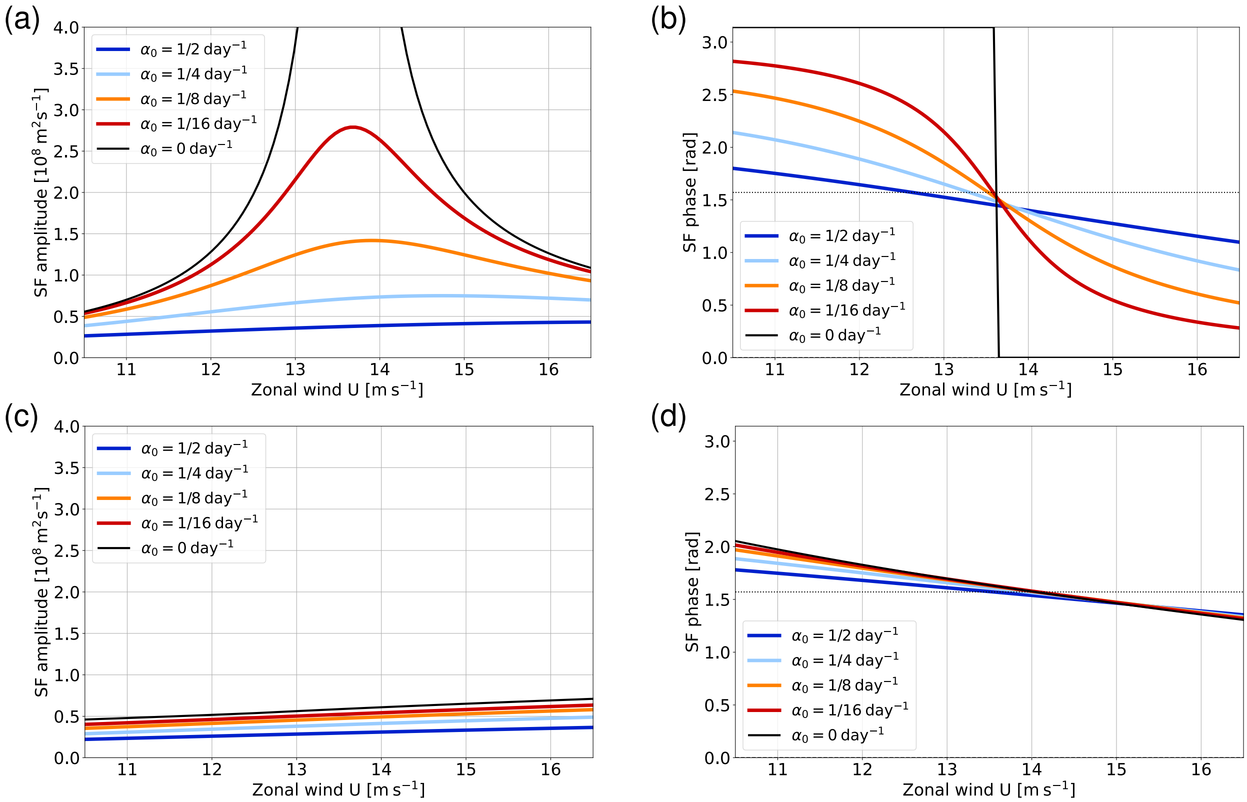

FIG. 10. Amplitude and phase behavior of the complex function $\psi_k(y)$ for the numerical solution in a channel with a constant basic state zonal wind U, as a function of U. The (a) amplitude (maximum value of the streamfunction ψ' in the channel) and (b) phase, for the fully reflecting boundaries. (c) amplitude and (d) phase for a sponge-leakage setup at the southern boundary of the notional channel (cf. the dashed line in Fig. D1b). In all panels, the different lines refer to different values of the constant damping coefficient α_0.

a. Exploring boundary conditions

Our boundary condition for ψ_k corresponds to perfect reflection at the northern and southern boundary of the computational domain. For illustration we compute the numerical solution for a constant $\overline{u} = U$ and various values of a constant damping coefficient $\alpha = \alpha_0$, as this allows comparison with our analytical solution. The result is provided in the top row of Fig. 10. Apparently, there is a strong similarity to our no-leakage analytical solutions (Fig. 2), showing a resonant peak at $U = 13.6\,\mathrm{m\,s^{-1}}$ and a jump in the phase of ψ_k for the undamped case. For increasing damping, the behavior gets increasingly smoother as expected. The pattern of the streamfunction is shown in Fig. 11a.

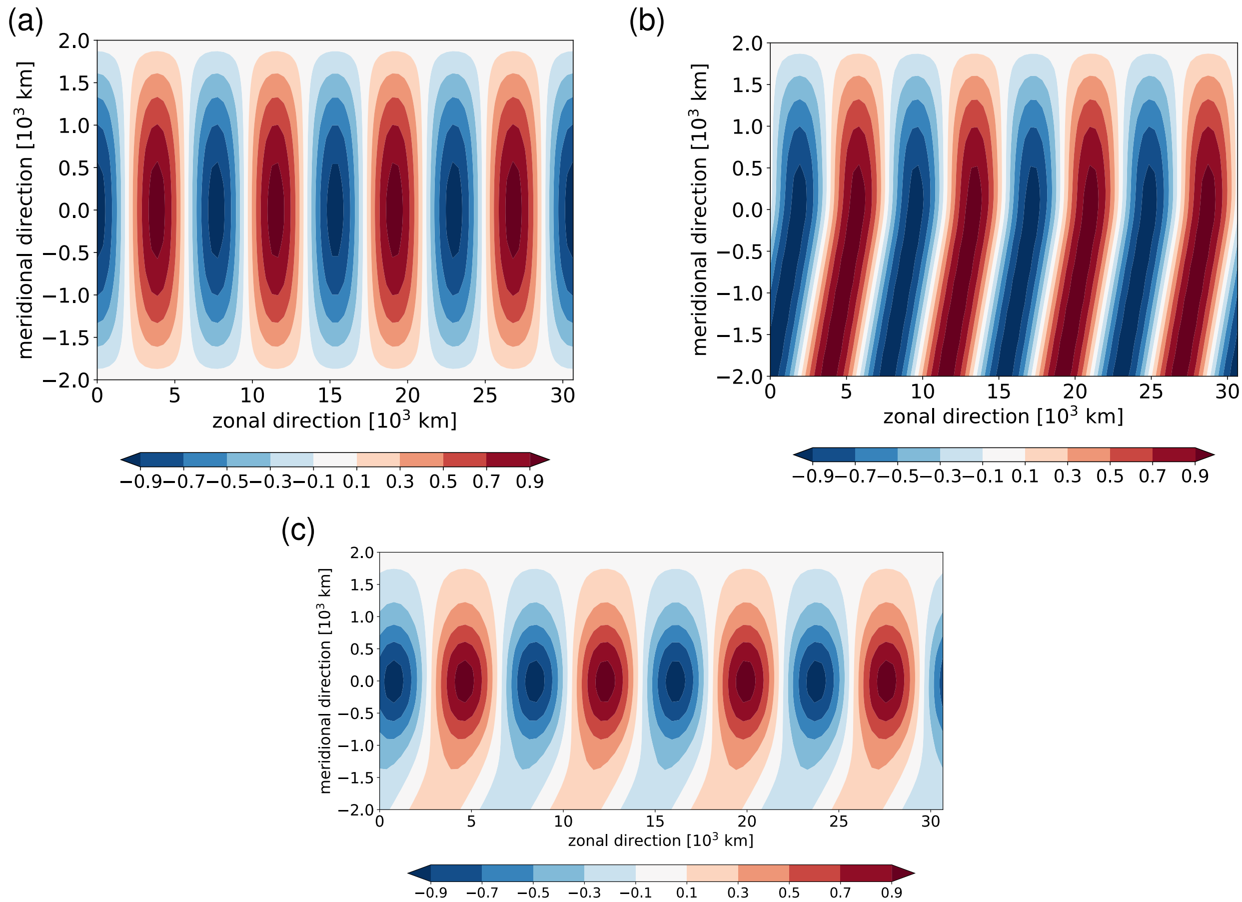

FIG. 11. Normalized streamfunction from the numerical solution with $s = 4$ and no damping for three different model configurations. (a) Standard configuration with perfectly reflecting boundaries and a constant basic wind $U = 13.6\,\mathrm{m\,s^{-1}}$; (b) same as panel (a) except that the southern boundary of the notional channel has effectively been replaced by a sponge-leakage condition; (c) configuration with the jet-like wind profile from Fig. 13a with a sponge-leakage southern boundary condition.

In our next step we aim to simulate a channel that allows wave activity to leak out at the southern boundary. Numerically this can be achieved by a so-called sponge in part of the computational domain; more specifically, the damping coefficient is judiciously specified as a function of latitude such that the wave activity is reduced to zero before the wave reaches the boundary; at the same time, the spatial increase of the damping coefficient must be gradual enough such that it does not lead to spurious reflection. To construct such a sponge layer, we use two different types of sponges, one with a cosine-like dependence on latitude and another one with a quasi-exponential dependence on latitude. The former is used for heuristic purposes, while the latter is meant to be used in all final applications. Details about the sponge design are provided in appendix B1.

Although generally the sponge technique is well established, we report here about a few experiments with our cosine-sponge (see Fig. D1a) in order to learn how to properly design the sponge for our purposes. In this set of experiments the sponge-free area is inviscid, i.e., $\alpha_0 = 0$. Varying the amplitude of the sponge α_s between 0.3 day^{-1} and 1000 day^{-1}, we obtain the result shown in Fig. 12a. The behavior for $\alpha_s = 0.3\,\mathrm{day}^{-1}$ is very similar to that shown in Fig. 10a (black line), indicating that the sponge is very weak and does not have a strong influence. By contrast, the result for the very strong sponge amplitude ($\alpha_s = 1000\,\mathrm{day}^{-1}$, red line) suggests that there is spurious reflection due to the strong spatial increase of the damping coefficient, resulting in resonant behavior at a lower value of U compared to $\alpha_s = 0.3\,\mathrm{day}^{-1}$. The two intermediate values of α_s (orange and light blue line) show a weaker resonant peak as well as a gradual shift in the location of the resonance. We interpret this as a situation in which the damping from the sponge effectively reduces the resonant amplitude, while the steepness of the sponge increasingly shifts the location of the resonance.

The shift in the location of the resonance to lower values of U for increasing sponge amplitudes α_s can be explained as follows. For a constant zonal basic wind and no damping, one expects resonance when the zonal and the meridional wavenumber satisfy $k^2 + l^2 = \beta/U$. Using the dimensionless wavenumbers s and n, one obtains

$$U_{\mathrm{res}} = \frac{\beta}{s^2\left(\frac{2\pi}{L_x}\right)^2 + n^2\left(\frac{\pi}{L_y}\right)^2} \tag{27}$$

as a prediction for the resonant value of U. The large-amplitude sponge effectively leads to reflection at the steep part of the sponge, which is inside the computational domain; thus, it effectively reduces the value of L_y, and this leads to a reduction of U_{res} according to (27).

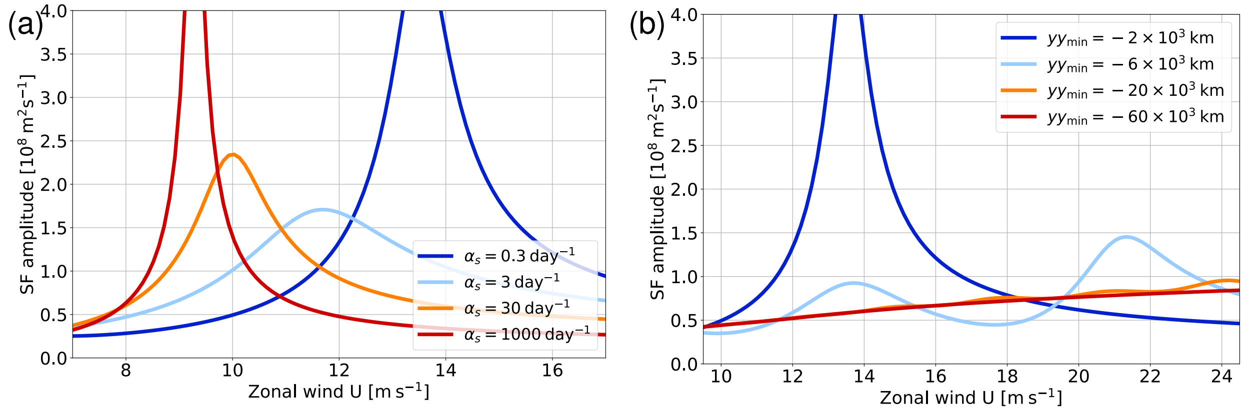

FIG. 12. Resonant behavior for $\alpha_0 = 0$ and various configurations of the cosine-shaped sponge (see Fig. D1a). Both panels show the maximum of the streamfunction ψ' in the sponge-free area as a function of the constant basic state zonal wind U, and the four lines in each panel represent the result for different parameter combinations that vary the strength and the steepness of the sponge. (a) Fixed channel width with $Y_{\min} = -2 \times 10^3$ km, but varying values for the sponge amplitude α_s; (b) fixed sponge amplitude $\alpha_s = 0.3$ day^{-1}, but varying channel width corresponding to different values of $Y_{\min}$.

There is an alternative way to increase the strength of the sponge that does not necessitate an increase of sponge amplitude: namely by keeping the sponge amplitude at a fairly low value ($\alpha_s = 0.3$ day^{-1}) and, instead, extending the computational domain further towards the south. The results of this set of experiments in shown in Fig. 12b. The curve for $Y_{\min} = -2 \times 10^3$ km (dark blue) is identical to the dark blue line in Fig. 12a (note that the two panels cover a different range of values for U). Increasing the channel width (light blue line) shifts the location of the dominant resonance towards a larger value of U (namely $U \approx 21.3\,\mathrm{m\,s^{-1}}$) and lowers the amplitude of the resonant peak owing to the increased damping with the more extended sponge. At the same time, a secondary resonant peak appears at $U \approx 13.7\,\mathrm{m\,s^{-1}}$, corresponding to the second meridional mode $n = 2$. Increasing the channel width even further (orange and red lines) keeps shifting the corresponding resonant peaks to larger values of U and makes even more peaks visible in the displayed range of values; however, at the same time the damping from the more extended sponge reduces the resonant peaks such that there is no longer any visible resonant behavior in the dark red curve. We conclude that the sponge design corresponding to the red line in panel b effectively simulates a fully-leaking boundary at $y = -2 \times 10^3$ km.

Having gained intuition into the sponge design with the help of the cosine-like sponge, we now switch to the quasi-exponential sponge, because the latter is better suited to obtain an efficient sponge. In addition, we now keep the area between $y = -2\times10^3$ km and $y = 2\times10^3$ km free of any sponge; at the same time we extend the computational domain southward to $Y_{\min} = -20\times10^3$ km and use a value of $\alpha_s = 1\,\text{day}^{-1}$. This sponge design is meant to be final and will be used in the remainder of this section.

The resulting behavior is shown in the bottom row of Fig. 10; it is drastically different from the behavior for the fully reflecting boundaries (shown in the top row of the same figure). The reason for this stark difference is that our quasi-exponential sponge effectively simulates a fully-leaking boundary at $Y_{\min} = -2\times10^3$ km, and apparently this eliminates any hint of resonant behavior in the amplitude and phase dependence on the zonal wind U, similar to the analytical solution for a fully-leaking channel (c.f. the $|R|^2 = 0$ lines in Fig. 3). The pattern of the streamfunction for $U = 13.6\,\text{m s}^{-1}$ is provided in Fig. 11b: northward of the forcing (i.e., for $y > 0$), the pattern looks quite like in the perfectly reflecting case (cf. Fig. 11a); however, southward of the forcing (i.e., for $y < 0$), there is a clear phase tilt consistent with southward propagation of wave activity. This is similar to the analytical solution (not shown, but see the similar structure for the case with 95% leakage in Fig. 5b.)

b. Basic state with a Gaussian jet

We now make use of the numerical model in order to investigate a basic state wind profile that varies with latitude. More specifically, we start with a constant zonal wind with strength $5\,\text{m s}^{-1}$ and superimpose a Gaussian jet with a standard deviation of 600 km and an amplitude of $25\,\text{m s}^{-1}$. As a result, we obtain a jet-like profile with the strength of the jet reaching $30\,\text{m s}^{-1}$ at $y = 0$ (Fig. 13a). The profile of the corresponding dimensionless stationary wavenumber $\hat{K}_s$ is shown in in Fig. 13b. According to WKB theory, the regions where $\hat{K}_s > s$ are wave propagation regions, where the solution assumes a wave-form, and there regions where $\hat{K}_s < s$ are wave-evanescence regions where the solutions are exponential. The latitudes at which $\hat{K}_s = s$ are turning surfaces, from which the waves are reflected back (obtained formally by asymptotic matching of the WKB solutions on both sides of the turning latitudes to an Airy function, c.f. Tung and Lindzen 1979b). The jet profile has a distinct relative maximum of $\hat{K}_s$ at $y = 0$, with $\hat{K}_s$ decreasing to zero and giving way to imaginary values in the northern and southern parts of the channel, and returning to real values near the channel walls, suggesting the wave-geometry of the problem is an inner waveguide in which we force the wave, flanked by evanescent regions, which are further flanked by additional external wave propagation regions which are bounded by the channel walls. If we ignore the outer wave propagation regions (by assuming, for example, that the flanks of the jet are modified to make the imaginary $\hat{K}_s$ regions essentially infinite), WKB theory suggests the waves would be fully reflected from turning latitudes, for any wavenumber $1 \leq s \leq 8$, resulting in a perfect waveguide with zero leakage (Hoskins and Ambrizzi 1993; Petoukhov et al. 2013; Kornhuber et al. 2017b). With the additional wave-propagation regions, some of the wave activity excited in the main waveguide will tunnel to walls (the exact amount depending on how wide the wave-evanescence region is relative to the exponential decay rate), from which they will be reflected back, yielding essentially a perfect waveguide. If on the other hand, we replace the southern wall with a sponge as constructed in the previous section, the wave activity which manages to tunnel out of the main waveguide southward will be fully absorbed, resulting, essentially in a leaky waveguide. Note that unlike the analytical model, the amount of wave activity leakage to the sponge depends on the structure of $\hat{K}_s$ and on s, and is thus not something we can control.

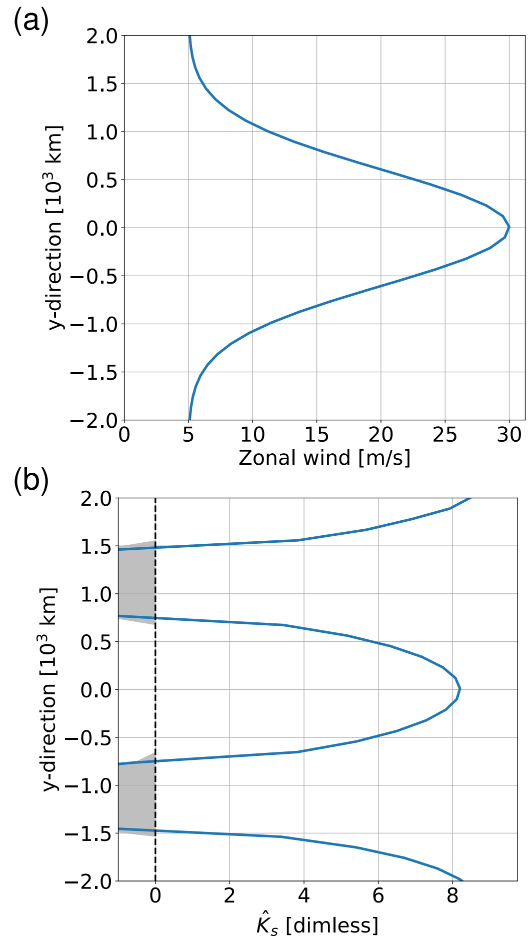

FIG. 13. Model configuration with a jet-like profile for the basic state wind. Panel (a) shows the zonal wind $\overline{u}(y)$, panel (b) shows the dimensionless stationary wavenumber $\hat{K}_s(y)$; negative values of $\hat{K}_s$ (gray shading) represent minus the imaginary part of $\hat{K}_s$.

To test this, we will evaluate the numerical solutions of this jet profile, with and without the sponge-leakage, for different values of α_0. In this set of experiments, we need to change our strategy for probing resonant behavior, because the wind is not a constant any longer. Instead, we simply vary the (dimensionless) zonal wavenumber s, which for the current purpose is not even limited to integer numbers. The result for the model configuration without sponge-leakage is shown in the top row of Fig. 14. Apparently, there is a resonant peak at $s \approx 4.3$ with the amplitude (panel a) of the undamped solution going to infinity and the phase (panel b) changing discontinuously from π to 0. Qualitatively, this behavior is very similar to the behavior shown in Fig. 10a and b, except that the method of probing for resonance has changed.

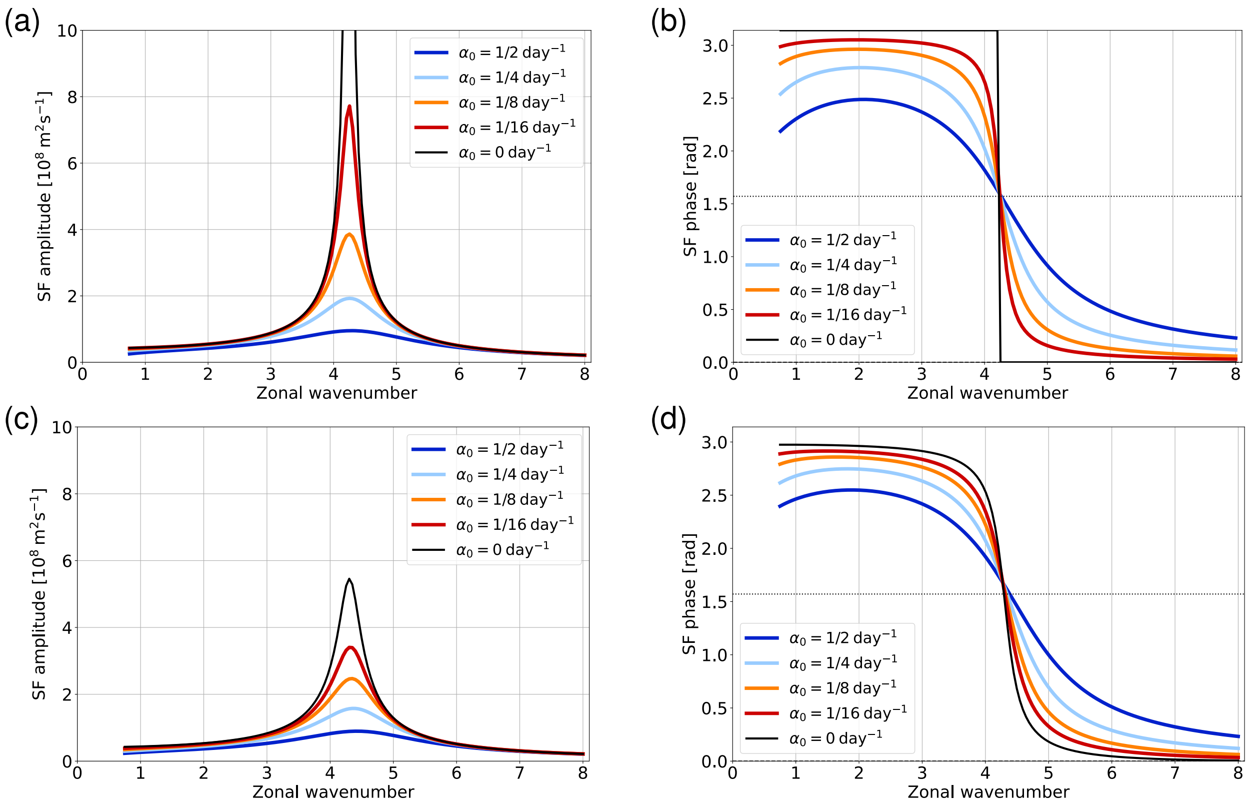

FIG. 14. Resonant behavior in case of our jet-like profile of the basic state wind (see Fig. 13). Top row: perfectly reflecting surfaces at the northern and southern boundary; bottom row: like top row except that the southern boundary condition has effectively been replaced by sponge-leakage. The left column shows the maximum value of the streamfunction ψ' as a function of s; the right column shows the phase of the complex function ψ_k at $y = 0$ as a function of s. The different colored lines refer to different values of the constant damping coefficient α_0.

We now repeat this simulation except that the southern boundary is replaced by the quasi-exponential sponge in a southward extension of the computational domain as detailed above and in the appendix. The result is shown in the bottom row of Fig. 14. As before, there is a clear peak of wave amplitude at $s \approx 4.3$ (panel c), which is likewise mirrored in the phase behavior (panel d). However, for the inviscid case ($\alpha_0 = 0$, black lines) our solution is not consistent with perfect resonance as predicted for a perfect channel: the amplitude does not tend towards infinity and the phase does not show a discontinuity. Instead, the behavior is broadly consistent with the analytical leaky-waveguide solutions (e.g. Fig. 3), as expected if indeed the southern turning latitude is not perfectly reflecting, but rather it allows some of the wave activity to leak out of the jet-waveguide.

The pattern of the streamfunction (Fig. 11c) is also qualitatively like the analytical leaky waveguide solution (Fig. 5b): it shows a phase tilt close to the southern boundary, indicating leakage of wave activity at $y = -2\times10^3$ km. As expected, some of the wave activity has tunneled through the area with imaginary $\hat{K}_s$ where it is slowly absorbed by the sponge essentially allowing wave activity to escape out towards $-\infty$.

Finally we compare the inviscid solution with sponge-leakage (black lines in Fig. 14c and d) with the damped solutions for a fully reflecting boundary (colored lines in Fig. 14a and b). This comparison suggests that the leakage of our jet-like profile is roughly equivalent to a damping with a 12 day time-scale. From comparing the phase change in tables 1 and 2, a 12 day damping time scale is equivalent to about 70% leakage (30% reflectivity). Again, arguments which assume perfectly reflecting boundaries on the basis of the existence of two turning latitudes are quantitatively deficient by a considerable margin.

5. Discussion

In this work we examine the influence of a specified amount of wave activity leakage to the equator, on the resonant response to idealized forcing. The main novelty of our analysis is that we derive an analytical solution with which we can quantitatively examine the effects of a specified amount of waveguide-leakage, and compare it to the effects of damping. The ability to explicitly specify the amount of wave activity leakage, and get an analytical solution comes at the price of large simplification of the problem. We thus use a numerical model, for which we carefully construct a fully-leaking southern boundary, to further examine the effect of leakage in a similar setup but with a meridionally varying jet, rather than a constant zonal mean zonal wind.

Using our analytical solution, we examine the resonant response to a forcing placed at the center of the waveguide, by varying the zonal mean flow incrementally across resonance. We vary separately and together, the amount of wave activity leakage (through the southern boundary condition) and the linear damping, to study their effect on the resonance behavior. Following are the main points to note about the analytical solution.

1. For inviscid flow on a perfect waveguide (no leakage to the equator), we get a sharp increase in the wave amplitude and a sharp π-phase change across resonance. Leakage acts to decrease the resonant amplification, and make the phase change more gradual across the resonance,

so that at 100% leakage the solution shows no amplification or increased phase change at the resonance values. Strong damping, on the other hand, weakens the response, which shifts towards larger zonal wind values. It does not eliminate the resonant response as full leakage does.

2. For a small wave activity leakage of magnitude $1-|R|^2$, the influence is similar to a damped wave with a damping rate corresponding to a loss of $1-|R|^2$ of the wave activity over the time it takes a wave packet to propagate the channel width back and forth with the theoretical group speed (calculated assuming no damping). For larger leakage, this gives an under-estimate of the effective damping rate.

3. The latitude-longitude structure of the response is very different between damping and leakage. Damping introduces a westward phase tilt on both sides of the forcing, corresponding to an outward-directed decaying EP flux (inward-directed momentum flux), which reduces to zero at the rigid-lid boundaries. Leakage from the southern boundary, on the other hand, introduces a westward phase tilt towards the southern boundary, south of the forcing, with no phase tilt poleward of it. This corresponds to no EP flux polewards of the forcing and a constant negative (southward) EP flux south of the forcing.

4. In addition to a main resonance peak, which occurs for the gravest meridional mode, we also get higher order resonance peaks, corresponding to the higher order meridional modes (we explicitly show the second mode peaks). We also find anti-resonance points, for which the meridional modes exactly cancel the forcing, resulting in a sharp amplitude decrease as the zonal mean zonal wind is gradually varied. The anti-resonance behavior involves a significant change in the meridional structure of the waves, specifically, the formation and shifting of meridional nodes, thus their appearance is sensitive to the latitude at which we sample the wave amplitude. In addition, the anti-resonance will vanish if the forcing has a meridional extent rather than a δ-function structure.

5. The above results can be reproduced by changing the zonal wavenumber or the channel width, rather than the zonal mean zonal wind value.

6. The analytical Green's Function solution can be extended to an arbitrary forcing structure, by using a Fourier transform for a zonally-varying forcing, and meridionally convolving the solution with the forcing for latitude variations.

To check if the main results hold for a meridionally varying jet, we implement leakage into a numerical β-plane channel model with linear damping, by adding a wide sponge layer to its southern edge, and exploring different zonal wind profiles and linear damping values. To check for a resonant response in these runs, we vary the zonal wavenumber. Following are the main results and conclusions from the numerical solutions:

1. Wave activity leakage to the equator can be implemented into the channel model by adding a gradual enough and wide enough sponge layer to the southern part of the domain. We verify the effect of such sponge-leakage by testing it on a constant zonal wind setup, and verifying that resonance disappears in a similar manner to the analytical solution with full leakage.

2. Adding a zonal jet to the model with no sponge reproduces a resonant behavior. However, when sponge-leakage is implemented at the southern boundary, outside the jet, beyond its southern flank, the resonance sharpness is considerably reduced, implying that the jet waveguide is leaky. Refractive index-based estimates that identify so-called turning surfaces, but don't take leakage into account (e.g. Petoukhov et al. 2013, and following studies), may overestimate the potential for resonance by a considerable margin.

The above solutions have allowed us to quantify and characterize the influence of wave-activity leakage to the equator in very idealized setups. More specifically, a rough estimate based on comparing the responses of the jets in the numerical runs with southern-boundary sponge-leakage and a wall, suggests the leakage of the jet is equivalent to a damping time scale of 12 days. In our analytical solution, a 12-day damping corresponds to a leakage of about 70% of the wave activity.

There are a few important subtleties to note. In the analytical model setup, we specify the reflection coefficient $|R|$, where $1-|R|^2$ is the *fraction* of wave activity that leaks out to the equator. Given, however, that the wave source is part of the solution, as it depends on the phasing between the wave and the topography, deducing $|R|$ from the wave solution itself involves solving a nonlinear equation, the form of which depends on the specifics of the forcing. Thus we were not able to derive a simple methodology to explicitly calculate the leakage from a given wave solution in a general circulation model or reanalysis for which the explicit forcing effect on the stream-function is not straightforward to obtain. Also, in the numerical solution with sponge-leakage and a jet, the amount of leakage depends on the zonal mean zonal wind profile, as well as the proximity of the equatorward turning surface to the sponge. Thus, unlike the analytical solution, we are not able to *specify* the amount of leakage in a numerical model.

A rough estimate of the leakage of a waveguide can be obtained from the ratio between the amount of wave activity which leaks to the equator (the meridional EP flux out of the southern waveguide boundary) and the source of wave activity in the wave guide. While the former is relatively straightforward to deduce, the latter is much more complex, as it depends on the physical process that excites waves, as well as the model setup and parameters. Nonetheless, several studies have obtained a rough estimate of the equatorward leakage, using analytical normal-mode solutions (Tung 1979) or idealized numerical model setups (Lutsko and Held 2016; Wirth 2020). The latter studies used a localized wave source to estimate the ratio between the amount of wave activity propagating into or remaining in the zonal waveguide, and that propagating or reaching equatorwards. These studies, as well as estimates from our numerical model (not shown) give estimates of at least 25% wave activity leakage even from a strong jet. More specifically, in Wirth (2020), a jet similar to that in our numerical simulations was estimated to have a waveguidability of about 60% meaning a leakage of about 40% (see figure 6a in Wirth 2020, for a jet strength of $25ms^{-1}$ and width of 5^o). This is smaller than our analytical-solution-based estimate of 70%, however, Wirth (2020) examined a jet on a sphere, and estimated the waveguidability using a forcing that is localized in longitude, thus, the reasons for this difference require further analysis.

Despite the limitations of the analytical solution, and the inability to explicitly calculate a leakage factor in realistic models and observations, the analytical solutions suggest that quite large leakage, in itself, does not preclude the possibility that quasi-resonant amplification can be significant enough to result in a significant impact on regional weather conditions. For example, assuming a damping rate of 8 days (which is quite strong for the upper troposphere), a change in the jet-waveguide which decreases the leakage from 100% to 50% can result in an amplification by about a factor of 2 at resonance, and by about 20% if the leakage changes from 50% to 25% (compare the peak values of the cyan - 100%, purple - 50%, and green - 25% curves in Fig. 6a). Also, even for a 75% leakage, the mid-channel amplitude can almost double if the zonal mean zonal wind changes by a few meters per second (see the amount of amplification of the green curve between $U = 11ms^{-1}$ and $U = 14.5ms^{-1}$ in Fig. 6a). While a doubling of the wave amplitude is very small in our model, in the real world it can be enough to cause extreme weather.

A main caveat in the relevance of our analysis to the real atmosphere is that the jet stream waveguide and the forcing are not zonally symmetric. In spite of this, circumglobal waves have been shown to dominate intra-seasonal variability (Branstator 2002). Kosaka et al. (2009) discussed the zonal structure and phasing of the circumglobal Northern Hemisphere summer Silk-Road pattern, and showed that the observed zonal phasing maximizes the energy conversion from the mean flow to the wave pattern, with the meridional energy conversion being most sensitive to the zonal phasing with respect to the zonal variations of the jet. The possibility of resonance playing a role in this sensitivity of the barotropic conversion remains to be studied. Circumglobal waves have been cited as the cause for the co-occurrence of extremes in several places around the globe (Davies 2015). Often, however, we see amplified zonal wave-packets leading to extreme weather (e.g. Feldstein and Dayan 2008; Röthlisberger et al. 2016, 2019; Fragkoulidis et al. 2018; Sandler and Harnik 2020; Ali et al. 2021), with a tendency of the waves to amplify in a specific region with a specific zonal phasing leading to extended or recurrent extreme weather (e.g. Röthlisberger et al, 2019; see figures 10, 12 in Fragkoulidis et al, 2018). Given that mathematically, wave packets are a superposition of a few close circumglobal modes, it remains to be examined if quasi-resonance of the carrier modes or the envelope modes can contribute to a zonally localized enhancement of waves.

Acknowledgments. The research leading to these results has been partly funded by the Transregional Collaborative Research Center SFB/TRR 165 "Waves to Weather" of the German Research Foundation (DFG), as well as the Israeli Science Foundation grants 1685/17 and 2466/23.

Data availability statement. The analysis was carried out solely based on the analytical solutions presented here (using MATLAB), and numerical stationary-wave solutions which were produced using software which is publicly available within the algorithm collection SciPy.

APPENDIX A

The approximate meridional wavenumber for the damped solution (equation 6)

.

Assuming weak damping, with a characteristic time scale much larger than the advective time scale, so that $\tilde{\alpha} \equiv \frac{\alpha}{kU} \ll 1$, we can approximate the meridional wavenumber using a Taylor expansion around the inviscid case:

$$\tilde{l} \approx \tilde{l}|_{\tilde{\alpha}=0} + \frac{\partial \tilde{l}}{\partial \tilde{\alpha}}|_{\tilde{\alpha}=0}\tilde{\alpha} \tag{A1}$$

Using equation 4:

$$\frac{\partial \tilde{l}}{\partial \tilde{\alpha}} = \frac{1}{2}\left(\frac{\beta}{U(1-i\tilde{\alpha})} - k^2\right)^{-1/2} \frac{i\beta}{U(1-i\tilde{\alpha})^2} = \frac{i\beta}{2\tilde{l}U(1-i\tilde{\alpha})^2} \tag{A2}$$

Plugging into A1, along with the definition of $\tilde{\alpha}$, noting that $\tilde{l}(\alpha = 0) = l$ (equation 5), and expressing in terms of the group velocity, $Cg_y = \frac{2kl\beta}{(k^2+l^2)^2} = \frac{2klU^2}{\beta}$, we get equation 6.

APPENDIX B

The boundary condition for a leaky waveguide

Starting from the expression in equation 13 for $G(y, y')$ at the southern part of the domain

$$G = B\left(|R|e^{i\tilde{l}(y+L)} - e^{-i\tilde{l}(y+L)}\right)$$

we get:

$$\frac{dG}{dy} = i\tilde{l}B\left(|R|e^{i\tilde{l}(y+L)} + e^{-i\tilde{l}(y+L)}\right)$$

At the southern boundary ($y = -L$) we thus have:

$$G = B(|R| - 1)$$

$$\frac{dG}{dy} = i\tilde{l}B(|R| + 1)$$

which gives the boundary condition 14.

B1. The non-leaky cosine-forcing solution

Starting with the inviscid model, we derive the solution 17 by plugging the Green's Function solution 16 into equation 2, for $h_k(y) = \cos(l_o y)$.

$$\psi'(y) = \int_{-L}^{L} G_k(y,y')h_k(y')dy' = -\frac{f_o}{l\sin(2lL)}\times \\ \left(\int_{-L}^{y}\sin(l(y'+L))\sin(l(y-L))\cos(l_o y')dy' + \int_{y}^{L}\sin(l(y'-L))\sin(l(y+L))\cos(l_o y')dy'\right) \tag{B1}$$

Examining only the first integral, after taking out the factor $\sin(l(y-L)$, we further develop, using the cosine and sine multiplication and addition/subtraction equalities:

$$\int_{-L}^{y}\sin(l(y'+L))\cos(l_o y')dy' = \\ -\frac{1}{2}\left(\frac{\cos((l(y+L)+l_o y) - \cos(l_o L)}{l+l_o} + \frac{\cos(l(y+L)-l_o y) - \cos(l_o L)}{l-l_o}\right) = \\ \frac{l}{l^2-l_o^2}\left[\cos(l_o L) - \cos(l(y+L))\cos(l_o y)\right] - \frac{l_o}{l^2-l_o^2}\sin(l(y+L))\sin(l_o y) \tag{B2}$$

repeating this derivation for the second integral in equation B1, plugging both back into B1, we find that the sine terms at the end of equation B2 cancel out in equation B1 between the two integrals, and doing further manipulation on the remaining terms, we get solution 17.

For the damped case, we can guess the solution to equation 3, by analogy with the inviscid solution 17, and noting that the following relation holds:

$$(\tilde{l}^2 - l_o^2)(1 - \frac{i\alpha}{kU}) = \frac{\beta}{U} - (k^2 + l_o^2) + \frac{i\alpha}{kU}(k^2 + l_o^2) \tag{B3}$$

where we used the full definition of $\tilde{l}^2$ (Equation 4), and not its approximation (Equation 6). The solution can then be verified by plugging into equation 3.

APPENDIX C

The EKE equation

Starting from the PV equation (c.f. equation 1):

$$\frac{\partial q'}{\partial t} + \overline{u}\frac{\partial q'}{\partial x} + v'\overline{q}_y + \alpha q' = -f_o\overline{u}\frac{\partial h}{\partial x} \tag{C1}$$

multiplying by ψ' and taking a zonal mean we get:

$$\overline{u}\,\overline{v'q'} - \alpha\overline{\psi'q'} = -f_o\overline{u}\,\overline{v'h} \tag{C2}$$

where overline denotes the zonal mean, and we used the relation between the streamfunction and the meridional velocity, $v' = \frac{\partial\psi'}{\partial x}$, and the fact that the zonal derivative of the zonal mean is zero, and that $\overline{\psi'v'} = 0$, and we assumed a steady state.

Next, we integrate over the entire meridional domain. We first note the following relation:

$$\int_{-L}^{L} \psi' q' dy = \int_{-L}^{L} \overline{\psi'\left(\frac{\partial v'}{\partial x} - \frac{\partial u'}{\partial y}\right)} dy = \int_{-L}^{L} \left(\overline{-v'\frac{\partial\psi'}{\partial x}} - \frac{\partial\overline{\psi'u'}}{\partial y} + \overline{u'\frac{\partial\psi'}{\partial y}}\right) dy =$$
$$- \int_{-L}^{L} \left(\overline{v'^2} + \overline{u'^2} + \frac{\partial\overline{\psi'u'}}{\partial y}\right) dy = 2EKE + \overline{\psi'u'}|_{-L} \tag{C3}$$

where $EKE \equiv \frac{1}{2}(\overline{v'^2}+\overline{u'^2})$, and we used the boundary condition $\psi'(L)=0$. Next noting that $\overline{v'q'} = -\frac{\partial \overline{u'v'}}{\partial y}$, thus

$$\int_{-L}^{L} \overline{v'q'}dy = \overline{u'v'}|_{-L}$$

where we use the boundary condition $v'(L)=0$. Plugging this, and equation C3 into equation C2, we get equation 22.

APPENDIX D

Design of the sponge

The sponge is modeled through a latitude-dependent damping coefficient $\alpha_{\mathrm{sp}}(y)$ such that the total damping coefficient is given by

$$\alpha(y) = \alpha_0 + \alpha_{\mathrm{sp}}(y)\ . \tag{D1}$$

Here, α_0 is a constant damping coefficient that may be considered in addition to the sponge. In the northern part of the channel we define a sponge-free area for $Y_S \leq y \leq Y_N$. South of Y_S the value of α_{sp} increases from α_0 to a user-specified value of α_s at the southern boundary of the computational domain.

In this work, $\alpha_{\mathrm{sp}}(y)$ is modeled either through a cosine-dependence or through a quasi-exponential dependence. The cosine-sponge is used in order to systematically explore the impact of the sponge on the resonant behavior. Based on experience thus obtained, we then designed a quasi-exponential sponge, which is used for our main results in order to efficiently simulate a non-reflecting (i.e., fully transparent) southern boundary of a notional channel that is less extended than the actual computational domain.

The cosine-like sponge simply connects the constant value α_0 in the sponge-free part of the domain with α_s at the boundary of the computational domain as illustrated in Fig. D1a.

The quasi-exponential sponge (see Fig. D1b) is specified such that $\alpha(y) = \alpha_s$ at the southern boundary of the computational domain. Obviously, the exponential function is non-zero for any real value of y, which implies that there cannot be any sponge-free area. In order to circumvent this issue and guarantee a truly sponge-free area in the northern part of the domain, we use the

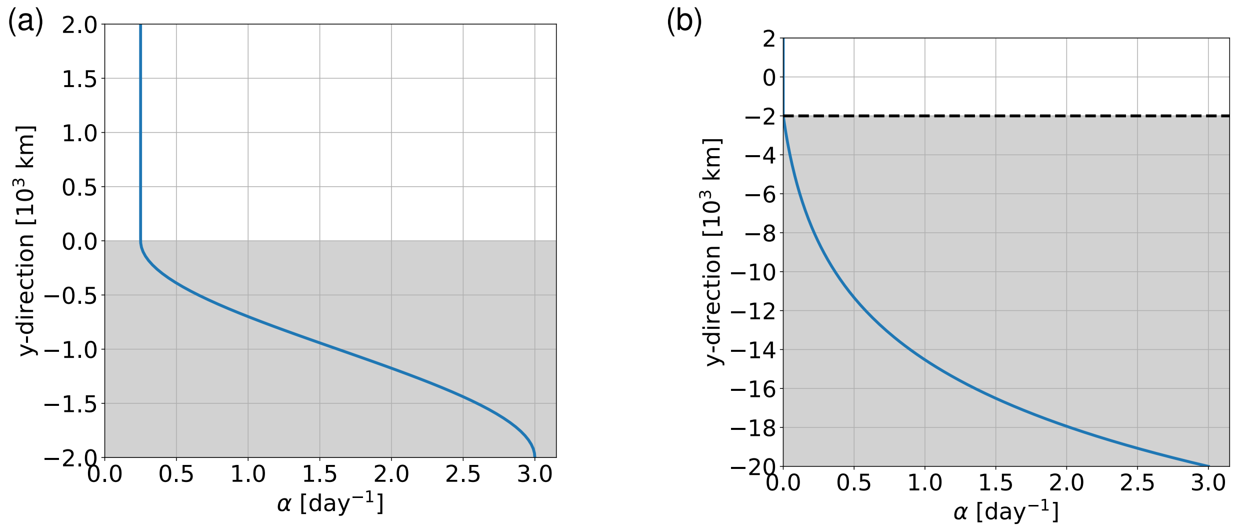

FIG. D1. Profiles of the damping coefficient $\alpha(y)$ for two different configurations that implement a sponge: (a) cosine-like sponge, and (b) a quasi-exponential sponge. For illustration we used here $\alpha_0 = 0.25\,\mathrm{day}^{-1}$ in panel (a), $\alpha_0 = 0$ in panel (b), and $\alpha_s = 3\,\mathrm{day}^{-1}$ in both panels. In addition, in both panels, the sponge-free area is white, while the sponge is marked by gray shading. The dashed line in panel b indicates the southern boundary of the notional channel, for which the sponge effectively simulates a fully-leaking boundary condition.

following algorithm resulting in a sponge that is close to exponential for typical values of α_0 and α_s used in this work:

1. We start with a true exponential function $\alpha_{\mathrm{sp}}(y) = a\exp(by)$ and determine the coefficients a and b such that α_{sp} equals $\alpha_{\mathrm{sm}} = 0.1\,\mathrm{day}^{-1}$ at the southern boundary of the sponge-free region, and $\alpha_{\mathrm{sp}} = \alpha_s$ at the southern boundary of the computational domain;

2. We subtract α_{sm} from the above-defined profile $\alpha_{\mathrm{sp}}(y)$ such that the damping of the sponge approaches zero as y approaches the sponge-free area

3. We multiply the function $\alpha_{\mathrm{sp}}(y)$ obtained in the previous step by a constant factor such as to ensure that the total $\alpha(y)$ equals α_s at the southern boundary of the computational domain.

The design of the exponential sponge is such that the sponge-free area is meant to represent the domain of interest. At the same time, the computational domain is extended towards the south in order to contain the exponential sponge. This combination effectively simulates a fully-leaking boundary condition at the southern end of the domain of interest (dashed line in Fig. D1b).

This shows how to enter the commands for making a bibliography using BibTeX. It uses references.bib and the ametsocV6.bst file for the style.

References

Ali, S., O. Martius, and M. Röthlisberger, 2021: Recurrent rossby wave packets modulate the persistence of dry and wet spells across the globe. *Geophys. Res. Lett.*, **48**, e2020GL091 452, https://doi.org/https://doi.org/10.1029/2020GL091452.

Branstator, G., 2002: Circumglobal teleconnections, the jet stream waveguide, and the North Atlantic oscillation. *J. Climate*, **15**, 1893–1910.

Charney, F. G., and J. G. DeVore, 1979: Multiple Flow Equilibria in the Atmosphere and Blocking. *J. Atmos. Sci.*, **36**, 1205–1216.

Coumou, D., V. Petoukhov, S. Rahmstorf, S. Petri, and H. J. Schellnhuber, 2014: Quasi-resonant circulation regimes and hemispheric synchronization of extreme weather in boreal summer. *Proc. Natl. Acad. Sci. (USA)*, **34**, 12 331–12 336.

Davies, H. C., 2015: Weather chains during the 2013/2014 winter and their significance for seasonal prediction. *Nature Geoscience*, DOI:10.1038/NGEO2561.

Esler, J. G., L. M. Polvani, and R. K. Scott, 2006: The antarctic stratospheric sudden warming of 2002: A self-tuned resonance? *Geophys. Res. Lett.*, **33**, L12 804, doi:10.1029/2006GL026 034.

Esler, J. G., and R. K. Scott, 2005: Excitation of transient rossby waves on the stratospheric polar vortex and the barotropic sudden warming. *J. Atmos. Sci.*, **62**, 3661–3682.

Feldstein, S. B., and U. Dayan, 2008: Circumglobal teleconnections and wave packets associated with Israeli winter precipitation. *Quart. J. Roy. Meteor. Soc.*, **134**, 455–467.

Fragkoulidis, G., V. Wirth, P. Bossmann, and A. H. Fink, 2018: Linking Northern Hemisphere temperature extremes to Rossby wave packets. *Quart. J. Roy. Meteor. Soc.*, **144**, 553–566, DOI:10.1002/qj.3228.

Harnik, N., 2001: The evolution of a stratospheric wave packet. *J. Atmos. Sci.*, **59**, 202–217.

Haurwitz, B., 1940: The motion of atmospheric disturbances on the spherical earth. *J. Mar. Res.*, **3**, 254–267.

Hoskins, B. J., and T. Ambrizzi, 1993: Rossby wave propagation on a realistic longitudinally varying flow. *J. Atmos. Sci.*, **50**, 1661–1671.

Hoskins, B. J., and D. J. Karoly, 1981: The Steady Linear Response of a Spherical Atmosphere to Thermal and Orographic Forcing. *J. Atmos. Sci.*, **38**, 1179–1196.

Jin, F.-F., and M. Ghil, 1990: Intraseasonal oscillations in the extratropics: Hopf bifurcation and topographic instabilities. *J. Atmos. Sci.*, **47**, 3007–3022.

Källén, E., 1997: On hysteresis-like effects in orographically forced models. *Tellus*, **37**, 249–257, https://doi.org/10.3402/tellusa.v37i3.11670.

Killworth, P. D., and M. E. McIntyre, 1985: Do Rossby-wave critical layers absorb, reflect or over-reflect? *J. Fluid Mech.*, **161**, 449–492.

Kornhuber, K., S. Osprey, D. Coumou, S. Petri, V. Petoukhov, S. Rahmstorf, and L. Gray, 2019: Extreme weather events in early summer 2018 connected by a recurrent hemispheric wave-7 pattern. *Environ. Res. Lett.*, **14**, 054 002, doi:10.1088/1748–9326/ab13bf.

Kornhuber, K., V. Petoukhov, D. Karoly, S. Petri, S. Rahmstorf, and D. Coumou, 2017a: Summertime planetary wave resonance in the Northern and Southern Hemispheres. *J. Climate*, **30**, 6133–6150.

Kornhuber, K., V. Petoukhov, S. Petri, S. Rahmstorf, and D. Coumou, 2017b: Evidence for wave resonance as a key mechanism for generating high-amplitude quasi-stationary waves in boreal summer. *Climate Dyn.*, **49**, 1961–1979, doi:10.1007/s00 382–016–3399–6.

Kosaka, Y., H. Nakamura, M. Watanabe, and M. Kimoto, 2009: Analysis on the dynamics of a wave-like teleconnection pattern along the summertime asian jet based on a reanalysis dataset and climate model simulations. *J. Meteor. Soc. Japan*, **87 (3)**, 561–580.

Luo, D., 1997: Low-frequency finite-amplitude oscillations in a near resonant topographically forced barotropic flow. *Dyn. Atmos. Oceans*, **26**, 53–72, https://doi.org/https://doi.org/10.1016/S0377-0265(96)00481-2.

Lutsko, N. J., and I. M. Held, 2016: The response of an idealized atmosphere to orographic forcing: Zonal versus meridional propagation. *J. Atmos. Sci.*, **73**, 3701–3718.

Mann, M. E., S. Rahmstorf, K. Kornhuber, B. A. Steinman, S. K. Miller, and D. Coumou, 2017: Influence of anthropogenic climate change on planetary wave resonance and extreme weather events. *Scientific Reports*, **7**, 1–10, doi:10.1038/srep45 242.

Mann, M. E., S. Rahmstorf, K. Kornhuber, B. A. Steinman, S. K. Miller, S. Petri, and D. Coumou, 2018: Projected changes in persistent extreme summer weather events: The role of quasi-resonant amplification. *Science Advances*, **4**, eaat3272.

Manola, I., F. Selten, H. de Vries, and W. Hazeleger, 2013: "Waveguidability" of idealized jets. *J. Geophys. Res.*, **118**, 10,432–10,440, doi:10.1002/jgrd.50 758.

Pedlosky, J., 1981: Resonant topographic waves in barotropic and baroclinic flows. *J. Atmos. Sci.*, **38**, 2626–2641.

Petoukhov, V., S. Petri, S. Rahmstorf, D. Coumou, K. Kornhuber, and H. J. Schellnhuber, 2016: Role of quasiresonant planetary wave dynamics in recent boreal spring-to-autumn extreme events. *Proc. Natl. Acad. Sci. (USA)*, **113**, 6862–6867.

Petoukhov, V., S. Rahmstorf, S. Petri, and H.-J. Schellnhuber, 2013: Quasiresonant amplification of planetary waves and recent Northern Hemisphere weather extremes. *Proc. Natl. Acad. Sci. (USA)*, **110 (14)**, 5336–5341, doi:10.1073/pnas.1222000 110.

Plumb, R. A., 1979: Forced waves in baroclinic shear flow. part 2: Undamped evolution near the baroclinic instability threshold. *J. Atmos. Sci.*, **36**, 205–216.

Plumb, R. A., 1981: Forced waves in baroclinic shear flow. part 2: Damped and undamped response to weak near-resonant forcing. *J. Atmos. Sci.*, **38**, 1856–1869.

Rossby, C. G., 1940: Planetary flow patterns in the atmosphere. *Quart. J. Roy. Meteor. Soc.*, **66**, 68–97.

Rossby, C. G., and collaborators, 1939: Relations between variations in the intensity of the zonal circulation and displacements of the semipermanent centres of action. *J. Mar. Res.*, **2**, 38–55.

Röthlisberger, M., L. Frossard, L. F. Bosart, D. Keyser, and O. Martius, 2019: Recurrent synoptic-scale Rossby wave patterns and their effect on the persistence of cold and hot spells. *J. Climate*, **32**, 3207–3226, 10.1175/JCLI–D–18–0664.1.

Röthlisberger, M., S. Pfahl, and O. Martius, 2016: Regional-scale jet waviness modulates the occurrence of midlatitude weather extremes. *Geophys. Res. Lett.*, **43**, 10,989–10,997.

Sandler, D., and N. Harnik, 2020: Future wintertime meridional wind trends through the lens of subseasonal teleconnections. *Weather Clim. Dynam.*, **1**, 427–443.

Stadtherr, L., D. Coumou, V. Petoukhov, S. Petri, and S. Rahmstorf, 2016: Record Balkan floods of 2014 linked to planetary wave resonance. *Sci. Adv.*, **2 (4)**, e1501 428, 10.1126/sciadv.1501 428.

Tung, K. K., 1979: A theory of stationary long waves. Part III: Quasi-normal modes in a singular waveguide. *Mon. Wea. Rev.*, **107**, 751–774.

Tung, K. K., and R. S. Lindzen, 1979a: A Theory of Stationary Long Waves. Part I: A Simple Theory of Blocking. *Mon. Wea. Rev.*, **107**, 714–734.

Tung, K. K., and R. S. Lindzen, 1979b: A Theory of Stationary Long Waves. Part II: Resonant Rossby Waves in the Presence of Realistic Vertical Shears. *Mon. Wea. Rev.*, **107**, 735–750.

Vallis, G. K., 2017: *Atmospheric and Oceanic Fluid Dynamics*. Cambridge University Press, 947 pp.

Wirth, V., 2020: Waveguidability of idealized midlatitude jets and the limitations of ray tracing theory. *Weather Clim. Dynam.*, **1**, 111–125, https://doi.org/10.5194/wcd–1–111–2020.